2012

Simulations of Non-Contact Creep in Regimes of Mixed Dominance

Maija Benitz
University of Massachusetts Amherst

SIMULATIONS OF NON-CONTACT CREEP IN REGIMES OF MIXED DOMINANCE

A Thesis Presented

by

MAIJA A. BENITZ

Submitted to the Graduate School of the
University of Massachusetts Amherst in partial fulfillment
of the requirements for the degree of

MASTER OF SCIENCE IN MECHANICAL ENGINEERING

February 2012

Mechanical and Industrial Engineering

SIMULATIONS OF NON-CONTACT CREEP IN REGIMES OF MIXED DOMINANCE

A Thesis Presented

by

MAIJA A. BENITZ

Approved as to style and content by:

Robert W. Hyers, Chair

Ashwin Ramasubramaniam, Member

David P. Schmidt, Member

Donald L. Fisher, Department Head
Mechanical and Industrial Engineering

ACKNOWLEDGMENTS

I would like to thank my advisor Prof. Robert Hyers for the opportunity to pursue my Master's degree. His kind support and guidance has allowed me to accomplish my goal. I would also like to thank my committee members Prof. David Schmidt and Prof. Ashwin Ramasubramaniam for their valuable input and advice.

My family has been a great source of encouragement throughout my studies. I thank them for all their love, and for always providing a healthy dose of humor. I would like to thank my friends for providing laughs and entertainment throughout the process. Thank you to all of my lab mates, it has been wonderful to work with all of you.

None of this would have been possible without support from the Sancheti Fellowship and the Massachusetts Space Grant Consortium.

ABSTRACT

SIMULATIONS OF NON-CONTACT CREEP IN REGIMES OF MIXED DOMINANCE

FEBRUARY 2012

MAIJA A. BENITZ

B.A., COLORADO COLLEGE

M.S.M.E., UNIVERSITY OF MASSACHUSETTS AMHERST

Directed by: Professor Robert W. Hyers

Improvement of high temperature applications relies on the further development of ultra-high temperature materials (UHTMs). Higher performance and efficiency is driving the need for improvements in energy conversion and propulsion systems. Rocket nozzles, gas turbine engines and hypersonic aircraft depend on a better understanding of a material's performance at high temperatures. More specifically, the characterization of creep properties of high temperature materials is required.

Conventional creep testing methods are limited to about $1700°C$. Non-contact methods have been developed, which rotate spherical samples up to 33,000 rotations per second. A load is supplied by centripetal acceleration causing deformation of the sample. Non-contact methods have been performed above $2000°C$. The induction drive developed in the previous work has decoupled temperature from rotation, greatly expanding the experimental testing range.

Creep mechanisms may involve dislocation motion or the diffusional flow of atoms. Creep may be dominated by dislocation glide, dislocation climb, or diffusional-flow mechanisms. Multiple creep mechanisms can be active in a sample, but one is often dominant in a given regime which depends on stress, temperature and grain size. This work studies the creep behavior of samples in regions of transition between dominating creep mechanisms, and the effect on the precision of the measurement.

Two finite element models have been developed in the current work. A two-dimensional Norton creep model replaces the more computationally expensive three-dimensional Norton creep model developed in the previous work. Furthermore, a two-dimensional Double Power Law model has been developed to simulate creep behavior of high temperature materials in regimes of mixed dominance. The two-dimensional Norton and Double Power Law models are used to identify and characterize creep in the regions of transition between dominating creep mechanisms. Simulations are analyzed to determine the effect of regimes of mixed dominance on the creep measurements of rotating samples of high temperature materials.

TABLE OF CONTENTS

LIST OF TABLES

Table **Page**

LIST OF FIGURES

Figure **Page**

CHAPTER 1

INTRODUCTION

Creep is a critical design factor for materials that experience service temperatures over roughly half their absolute melting point. High temperature applications include heat exchangers, furnace linings, jet engine exhaust systems, and component for gas turbines. Due to the limitations of materials at high temperatures, including the susceptibility to creep, hot corrosion, oxidation, fatigue and microstructural instability, the thermodynamic efficiencies of most combustion engines have reached a maximum. Efficiencies can be improved by creating a new class of materials to withstand higher operating temperatures. State of the art technologies for rocket nozzles, hypersonic aircraft, and jet engines depend on the development of ultra-high temperature (UHT) materials. To meet this demand, materials including novel superalloys, and ultra-high temperature ceramics including carbides, nitrides, borides and silicides are being developed.

Tungsten light bulb filaments, which operate at $2500°C$ or higher, are a common household application in which creep resistance plays a major role. A functional incandescent filament must satisfy two basic requirements. First, the filament must resist creep deformation. The second requirement is resistance to creep fracture, which, is not accomplished as easily. A transient non-uniform thermal expansion occurs when the light bulb is turned on, causing a tensile force along the wire axis. The force is perpendicular to grain boundaries, and can lead to fracture on these boundaries. Fracture must then be prevented by delaying recrystallization of the grains. This is met by the addition of potassium which is inert in tungsten. Therefore, potassium lies

on grain and sub-grain boundaries where it restricts growth of recrystallized grains. Light bulb filaments are just one of the many examples of applications that require resistance to creep at high temperatures.

Gas turbines operate at elevated temperatures and also require resistance to creep deformation. It is necessary that the moving components do not fracture or creep at a significant rate. Furthermore, engine efficiency increases with higher operating temperature. This can only be achieved through significant improvement in high temperature capabilities of metals. Modern jet engines operate at $1200°C$ or higher, which includes the effects of intricate cooling systems. The efficiency of a gas engine is limited to 38% for a gas entry temperature of $926.85°C$, and increases to over 50% for entry temperature of $1526.85°C$ [39]. Heat resistant materials, generally referred to as superalloys, are required for the further development of high temperature engines.

Rocket nozzles are non-rotating components that also require creep resistance at very high temperatures. Nozzles experience low stresses, but at temperatures much greater than $1600°C$. Cobalt superalloys are commonly used for nozzle applications, as well as for other static components. Improvements to rocket nozzle technology depends on the development of UHT materials.

Another ultra-high temperature application that depends on creep resistance is hypersonic aircraft, aircraft that operate at Mach 5 or higher. The high temperature material requirements for the engines of hypersonic aircraft are the same for engines of land based vehicles and subsonic aircraft. With hypersonic aircraft, there is the added concern of the aircraft body temperature. Considerable heating occurs on the leading edge of the wing, due to adiabatic compression of the air, as well as atmospheric friction.The structural materials become weak at elevated temperatures, further driving the need for improvements in high temperature materials.

The development of non-contact creep testing has allowed high temperature measurements that were previously limited to $1700°C$ by conventional methods. Elec-

trostatic levitation (ESL) methods have processed samples above $3400°C$, with creep measurements up to $2350°C$. These testing methods are reviewed in Chapter 3. Research has been conducted on Nickel based superalloys funded by J2X, subcontracted by Pratt & Whitney Rocketdyne. Studies of non-metals, including ZrB2 have also been conducted, with funding from the Air Force and the Naval Surface Warfare Center. Additionally, niobium studies have been carried out by NASA at the Marshall Space Flight Center.

This research presents finite element analyses of non-contact creep deformation of a rotating sphere. Two FEA models have been developed to address creep deformation due to a single mechanism, as well as multiple mechanisms. These models are discussed further in Chapter 4. Various physical mechanisms control the rate of creep, including dislocation motion and diffusional flow of atoms. The dominating creep mechanism depends on the applied stress, temperature and grain size. The FEA models are validated against experimental results. The validated models are used to simulate the deformation of the sphere in regimes of mixed dominance. Further analyses are done to identify and characterize the region of mixed creep dominance, and are discussed in Chapter 5.

CHAPTER 2

CREEP PHENOMENA

Creep is the time-dependent permanent deformation that occurs at stresses well below the yield strength of a material. The deformation is seen in both crystalline and non-crystalline materials. Crystalline materials experience dislocation creep, while both crystalline and non-crystalline materials undergo diffusional creep. Higher temperatures give rise to greater mobility of dislocations, atoms and vacancies. Deformation by creep becomes significant above half the melting point of the material.

Creep consists of three stages, as shown in Figure 2.1. During Stage I, transient creep is observed. The strain rate decreases with time and strain. The change in the microstructure at high stresses behaves analogously to work hardening at lower temperatures. The strain rate decreases until it reaches the minimum creep rate, transitioning into Stage II. The secondary creep region is called the steady-state region, as the strain rate maintains a constant value consistent with the minimum creep rate. The strain rate remains constant because recovery of the microstructure occurs alongside deformation. In this region thermal energy activates cross-slip and climb (screw and edge dislocations, respectively, changing planes to circumvent obstacles), allowing recovery of the material to balance with its work-hardening capacity. Both cross-slip and climb increase the degree of freedom of dislocation motion. Tertiary creep is the final stage, in which the creep rate increases until fracture. Under a constant true stress, the microstructure undergoes changes, including recrystallization, coarsening of second-phase particles and nucleation of voids and microcracks. Steady

state creep is the region of interest for design purposes, and will be the focus of this research.

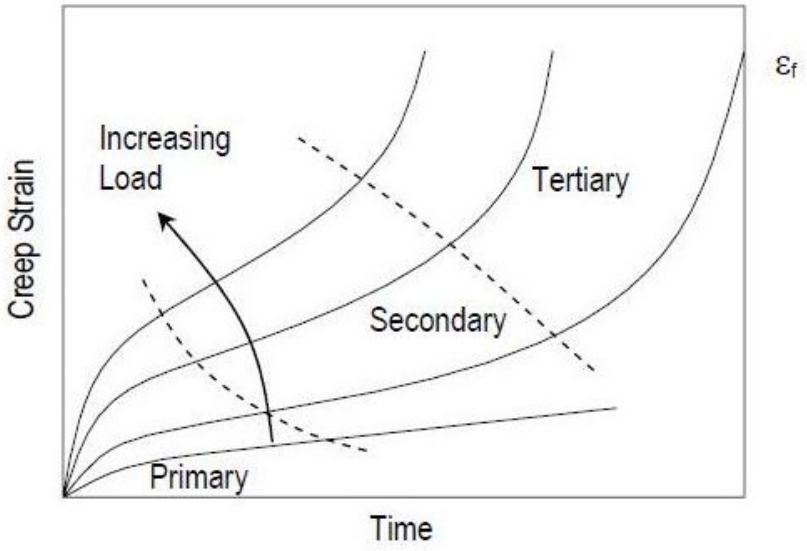

Figure 2.1. Strain versus time in a constant-stress creep test. Primary (transient creep): strain rate decreases with time and strain. Secondary stage (steady-state): strain rate constant. Tertiary creep: strain rate increases until fracture. [12]

Several mechanisms contribute to the creep of crystalline materials involving dislocation motion. Other mechanisms involve only the diffusional flow of atoms. Depending on temperature and applied stress, creep may be dominated by dislocation glide, dislocation climb, or diffusional-flow mechanisms. The combination of applied stress, temperature, and grain size determines the dominating creep mechanism of a material. Power-law (PL) creep is due to the motion of dislocations under high stress. PL creep depends on both stress and temperature. At high temperatures deformation can occur under very low stresses, and at low temperatures dislocation motion can occur under high stresses. Nabarro-Herring (NH) creep involves diffusion of atoms inside grains and along grain boundaries at high temperatures. Coble creep occurs on grain boundaries, and can take place at lower temperatures than NH.

These mechanisms, and a few others, will be discussed further in this remainder of this chapter.

2.1 Creep Mechanisms

2.1.1 Dislocation Creep

First dislocation motion and the role of temperature and stress in the determination of the creep rate will be considered.

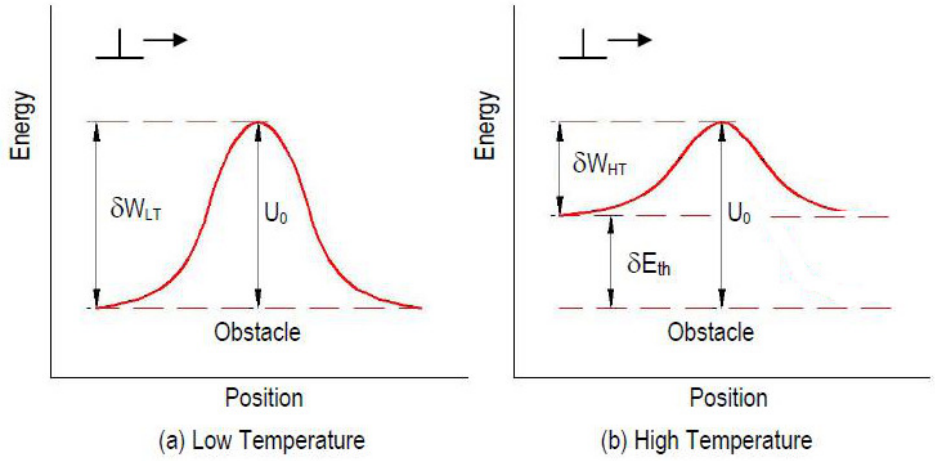

Figure 2.2. Energy-position curve. a) At low temperatures the dislocation is equally satisfied on either side of the obstacle. b) At high temperatures thermal energy reduces the amount of work needed to overcome the obstacle. Adapted from [12]

In determining the creep rate due to dislocation motion, we must consider the energy-distance curve for a dislocation approaching a barrier. For the case of no applied stress, the energy variation is symmetric with respect to each side of the energy barrier. That is, the dislocation is equally satisfied on either side of the obstacle. However, in the case of an applied stress driving the dislocation past the barrier, the energy curve is no longer symmetric about the obstacle. The energy is lower after the dislocation passes the obstacle. The difference between the initial energy and the final energy can be called δW. Part of this energy required to overcome the obstacle

can be supplied thermally (δE_{th}), exhibiting the dependence on both temperature and stress. The creep rate for dislocation glide is given by

$$\dot{\epsilon}_{DG} = \dot{\epsilon}_0 \exp(\frac{-U_0}{kT}) \exp(\frac{\tau bA}{kT}) \tag{2.1}$$

where, $\dot{\epsilon}_0$ is a material constant related to the frequency of atomic vibrations, U_0 is energy required to overcome the obstacle, k is Boltzmann's constant, T is the temperature, τ is the applied stress, b is the Burgers vector and A is the area on the slip plane. The first exponential term represents the intrinsic activation energy, and the second the stress assisted component. The second term is the ratio of the stress assisted energy over the thermal energy. As this ratio grows the creep rate increases.

2.1.2 Diffusional Creep

At lower stresses and higher temperatures, atomic diffusion dominates creep behavior. Diffusional creep does not involve dislocation motion as discussed in the previous section, and therefore requires a different analysis of the process.

Nabarro-Herring creep involves only atomic diffusion resulting in mass transport. To analyze the motion of atoms through a crystalline grain, a rectangular sample under lateral compression and vertical tension is considered, as shown in Figure 2.3. The vacancies diffuse into the bulk of the material under an applied stress. Meanwhile, interstitial atoms form additional layers on the grain boundaries perpendicular to the tensile axis, resulting in mass flux. Excess vacancies diffuse to grain boundaries parallel to the tensile axis, thus elongating the sample. The changing shape of the grain is driven by the vacancy gradient concentration, and as the grain elongates, creep deformation occurs. An analysis of the vacancy concentration and mass transport through the grain gives way to an expression for the strain rate due to Nabarro-Herring creep,

$$\dot{\epsilon}_{NH} = A_{NH}(\frac{D_L}{d^2})(\frac{\sigma\Omega}{kT}) \tag{2.2}$$

where A_{NH} is a constant that depends on geometric specifications, D_L is the lattice self-diffusion, d is the grain size, and Ω is the atomic volume. Nabarro-Herring creep is more important in ceramics than metals because dislocation motion is difficult in ceramics.

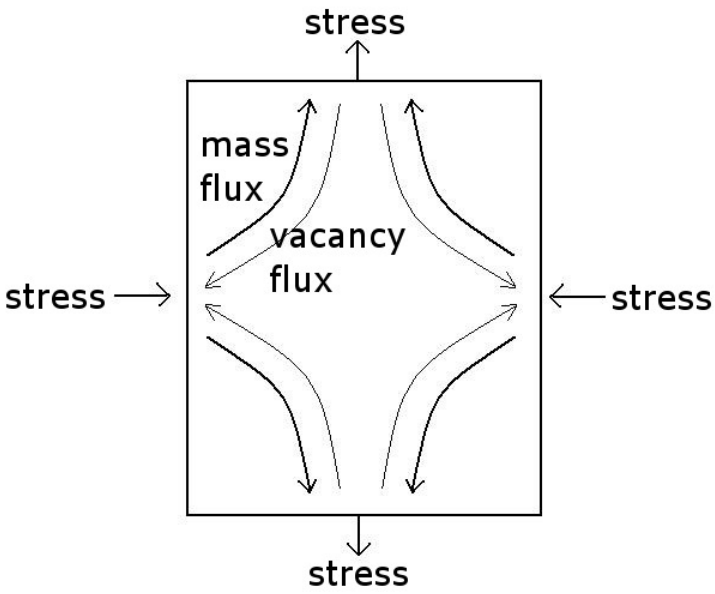

Figure 2.3. Schematic of rectangular sample under vertical tension and lateral compression, experiencing mass and vacancy fluxes in opposite directions.

Coble creep is also driven by the vacancy concentration gradient. However, mass transport in Coble creep occurs by diffusion along grain boundaries in polycrystals and along edges of single crystals, as opposed to Nabarro-Herring creep in which mass transport occurs through the bulk. By similar analysis of vacancy concentration gradients and mass transport, an expression for Coble creep rate is given by,

$$\dot{\epsilon}_C = A_C(\frac{D_{GB}\delta'}{d^3})(\frac{\sigma\Omega}{kT}) \tag{2.3}$$

where the diffusion area is proportional to $\delta^{'}d$, in which $\delta^{'}$ is the effective grain boundary thickness where mass transport occurs. Again, A_C is a constant that depends on geometrical factors, and D_{GB} is the diffusivity along grain boundaries.

Largely, Coble and Nabarro-Herring creep are quite similar in their dependence on applied stress and temperature. However, they differ in their respective sensitivity to grain size. Coble creep is more sensitive to grain size than Nabarro-Herring, as seen in the expression for creep rate. Thus Coble creep is more important in the creep behavior of finely grained materials. Nabarro-Herring and Coble creep are parallel processes, meaning they occur independently of each other. The total diffusional creep rate is then just the sum of the two processes, $\dot{\epsilon}_{total} = \dot{\epsilon}_C + \dot{\epsilon}_{NH}$. Further discussion of parallel and sequential processes will be provided later.

Harper-Dorn creep shares many of the same properties of diffusional creep, but results in a much larger strain rate. Furthermore, it lacks dependence on grain size. Experiments carried out by Harper and Dorn using aluminum at $0.99T_m$ found a proportional relationship between strain rate and stress, indicative of diffusional creep, however with strain rates 1400 times greater than expected [38]. In diffusion creep, deformation usually occurs around grain boundaries. By scribing lines into samples a stepwise deformation should be found along grain boundaries. Harper and Dorn instead found uniform deformation along grain boundaries and on the interior of the grains. Furthermore, the steady state creep rates for single crystal and polycrystalline aluminum were found to be the same. Despite the agreement of stress exponent and activation energy between Nabarro-Herring creep and the experimental data, there remained a discrepancy between strain rate and grain size dependence.

Pipe diffusion is another diffusional creep mechanism, which in certain circumstances can be the rate controlling mechanism. This mechanism involves the diffusion of vacancies along cores of dislocations. The area available for diffusion is now proportional to $\rho d^2 b^2$, where ρ is the dislocation density and b is the interatomic spacing.

The expression for pipe diffusion is found by multiplying the Nabarro-Herring creep rate by the ratio of the area available for pipe diffusion to bulk diffusion, giving,

$$\dot{\epsilon}_P = A_P(D_L\rho b^2)(\frac{\sigma\Omega}{kT}) \tag{2.4}$$

Again, the creep rate is proportional to the stress as it was for Nabarro-Herring and Coble creep, assuming that ρ is independent of σ. Most conditions gives $\rho \propto \sigma^2$, which would make the pipe diffusion creep rate proportional to σ^3, which is often referred to as power law creep.

2.1.3 Power Law Creep

At moderately applied stresses the creep rate is proportional to the stress raised to a power. When creep deformation involves both dislocation motion and diffusion flow we call the process power law creep. A basic power law of creep is given by,

$$\dot{\epsilon}_p = A(\frac{D}{d^2})(\frac{\sigma}{G})^n \tag{2.5}$$

where A is a geometrical factor, D is the diffusivity, d is the grain size, σ is the stress, G is the shear modulus and n is the stress exponent which describes the stress dependence and is determined by the creep mechanism at a given temperature.

Two mechanisms that fall under the umbrella of power law creep will be discussed here, they are solute-drag and climb-glide creep. Solute drag creep relates to solid solution strengthening. The size difference between solute atoms and edge dislocations restricts dislocation motion. At low temperatures the solute atoms are immobile, but at higher temperatures become mobile. At moderate velocities the solute atoms move with the edge dislocations, imposing a drag on the motion of the dislocation. The amount of drag acting on the dislocation depends on three factors; the solute atom diffusivity, size misfit parameter and solute atom concentration. These factors all contribute to the velocity of the dislocation, given by

$$v \sim \frac{(D_{sol}\sigma)}{(\epsilon_b^2 c_0)} \tag{2.6}$$

where D_{sol} is the diffusivity of the solute, ϵ_b^2 is the misfit parameter and c_0 is the solute atom concentration. Defining the creep rate as $\dot{\epsilon} = \rho b v$, where ρ is the dislocation density which is proportional to the stress squared, we arrive at the following expression for solute-drag creep rate.

$$\dot{\epsilon}_{SD} = A_{SD}(\frac{D_{sol}}{d^2})(\frac{\sigma\Omega}{kT})(\frac{\sigma}{G})^2 \tag{2.7}$$

Again A_{SD} is dependent on geometric factors and G is the shear elastic modulus. The same stress-volume temperature ratio that was seen in the diffusional creep equations is present, as well as an additional stress term not seen earlier. Solute-drag creep is therefore more sensitive to stress than Nabarro-Herring and Coble creep.

Climb-glide creep occurs when the applied stress is too low for the dislocation to overcome an obstacle. Instead of moving past the obstacle by dislocation glide, the dislocation must climb past the barrier. The dislocation then continues to glide until a new obstacle is encountered, in which it must climb again. This mechanism involves both climb and glide which occur sequentially. The overall creep rate is determined by the lesser of the two rates, which in this case is usually the climb rate. As before, the strain rate is defined as $\dot{\epsilon} = \rho b v_g$, where v_g is the glide velocity. Dislocation climb is driven by an applied stress and accomplished by diffusional flow. The creep rate is given by

$$\dot{\epsilon}_{CG} = A_{CG}(\frac{D_L}{h^{3.5}M^{1/2}})(\frac{\sigma\Omega}{kT}) \tag{2.8}$$

Assuming that h, the height of the climb distance is proportional to $1/\sigma$ and M, the sources per unit volume, is constant, the creep rate is then $\dot{\epsilon}_{CG} \sim \sigma^{4.5}$.

Many creep models have been posed that fit the general formulation of Power Law creep. Of these models, many are experimentally driven and lack theoretical

foundation. The stress exponent, n, is roughly equal to 3 for solid solutions and between 4 and 5 for pure metals [39]. Generally, stress exponents lie between 1 and 10. Eventually, a region called power-law breakdown is reached when the applied stress causes the creep rate to increase at a rate larger than any power of σ.

2.1.4 Summary of Creep Mechanisms

The assortment of creep mechanisms discussed thus far does not encompass all possible mechanisms, but should suffice as a general overview. While there is a great variety in equations describing the creep rate for different mechanisms, it should be noted that each one has in common a diffusivity term and a $(\sigma\Omega)/(kT)$ term, or more generally a stress assisted energy to thermal energy ratio.

Dislocation:

$$\dot{\epsilon}_{DG} = \dot{\epsilon}_0 \exp(\frac{-U_0}{kT}) \exp(\frac{\tau b A}{kT}) \tag{2.9}$$

Nabarro-Herring:

$$\dot{\epsilon}_{NH} = A_{NH}(\frac{D_L}{d^2})(\frac{\sigma\Omega}{kT}) \tag{2.10}$$

Coble:

$$\dot{\epsilon}_C = A_C(\frac{D_{GB}\delta'}{d^3})(\frac{\sigma\Omega}{kT}) \tag{2.11}$$

Solute Drag:

$$\dot{\epsilon}_{SD} = A_{SD}(\frac{D_{sol}}{d^2})(\frac{\sigma\Omega}{kT})(\frac{\sigma}{G})^2 \tag{2.12}$$

Climb-glide:

$$\dot{\epsilon}_{CG} = A_{CG}(\frac{D_L}{h^{3.5}M^{1/2}})(\frac{\sigma\Omega}{kT}) \tag{2.13}$$

Each of the creep mechanisms can be active, but vary over different orders of magnitude. Typically one of the processes will dominate in the creep deformation.

All of the creep mechanisms discussed above can be synthesized into one general expression for the creep rate. The factors pertaining to each of the creep mechanisms are listed in the table below. Nabarro-Herring and Coble creep both have a dependence on grain size, as shown by the value of n in the table. Power law creep has

an additional stress component, in which the exponent ranges between 2 and 6. This factor is absent in the diffusional flow creep mechanisms, making them less sensitive to stress. The overall creep rate expression is given by

$$\dot{\epsilon} = A(\frac{D}{\Omega^{2/3}})(\frac{\sigma}{G})^{m''}(\frac{\sigma\Omega}{kT})(\frac{b}{d})^{n} \tag{2.14}$$

The diffusivity-atomic volume term has units of 1/s, the same units as strain rate. The stress-volume temperature term demonstrates the role of stress and temperature in creep. Finally, the last term represents the grain size dependence of creep. The values in the table demonstrate the dependence on grain size for Nabarro-Herring and Coble creep, but not for Power Law Creep. Furthermore, Nabarro-Herring and Coble creep rates are linear with respect to the applied stress, unlike Power Law creep.

Table 2.1. Parameters in the general creep rate equation.

Mechanism	**Conditions**	**A**	**m"**	**n**
Nabarro-Herring	High T, low stress, fine grain	7	0	2
Coble	Lower T than NH, low stress, finer grain	50	0	3
Power Law	High stress	Varies	2-6	0

2.2 Independent and Sequential Processes

The mechanisms discussed above can all be active but dominate in different regimes of stress and temperature. In order to understand their relation to each other, the ways in which the creep mechanisms operate in conjunction must be discussed. Independent processes operate in parallel, while sequential processes operate in series. In parallel processes the larger of the creep rates dominates, and in sequential processes the lesser rate determines the overall rate.

Nabarro-Herring and Coble creep act in parallel, so their total creep rate is just the sum of the two mechanisms. The grain size determines which mechanism is dominant. Coble creep is proportional to d^{-3} while Nabarro-Herring scales with d^{-2}, making

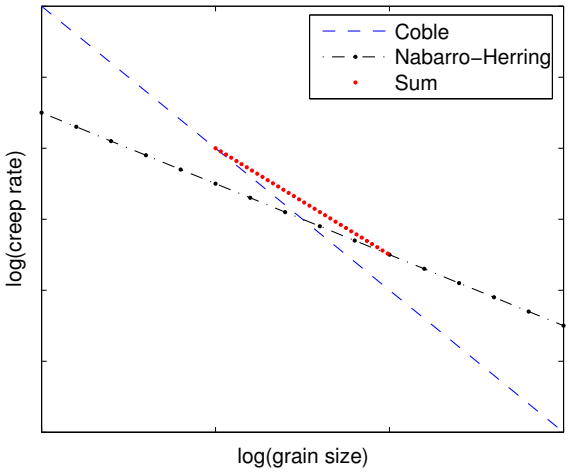

Figure 2.4. Nabarro-Herring and Coble creep rate dependence on grain size. Depending on the size of the grain, one mechanism dominates over the other.

Coble creep more sensitive to small grain sizes. The transition from one dominant regime to another as the grain size changes from small to large is illustrated in Figure 2.4.

Diffusional flow and dislocation creep are also independent mechanisms that take place in parallel at stresses and temperatures where both processes are present. Again, the greater creep rate dominates and is the determinant of the overall creep rate. The sum of the different mechanisms comprises the overall creep rate, which is given by $\dot{\epsilon} = \dot{\epsilon}_{dis} + \dot{\epsilon}_{diff}$. There exists a critical stress at which a transition from one mechanism to another occurs. The top curve in each regime graphically depicts the greater of the creep rates dominating, and can be seen in Figure 2.5.

Up until now there has been no discussion of a sequential process in which the lesser of the creep rates is the determining net rate. One instance of a sequential process is grain boundary sliding, which takes place in polycrystalline diffusional flow creep mechanisms, and is shown schematically in Figure 2.6. In diffusional creep, such as Nabarro-Herring or Coble, grains deform via mass transport. As the grains

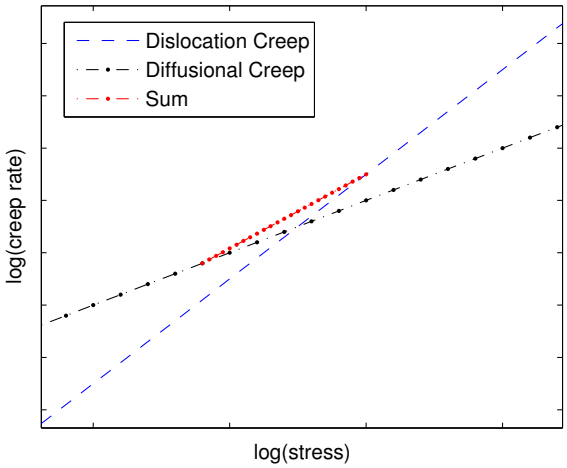

Figure 2.5. Schematic of creep rate-stress relationship for dislocation and diffusional creep mechanisms.

elongate in one direction and contract in the other, internal cracks and voids would be formed between grains. Grain boundary sliding prevents the formation of internal cracks and voids. The grain-boundary sliding prevents the creation of voids that could be formed due to polycrystalline diffusional creep. Grain boundary sliding can be considered sequential to diffusional flow. The grain boundary sliding occurs on a much smaller scale than on the polycrystalline grain level, and generally at a rate that is rapid enough to accommodate diffusional flow. Without rapid enough grain boundary sliding voids will form, which marks the onset of creep fracture. Since the process can be thought of as sequential, the net creep rate is the slower of the two, which in this case is the grain-boundary sliding rate.

2.3 Double Power Law Creep

To study the creep deformation in regimes of mixed dominance an equation that addresses multiple mechanisms is required. The steady state creep rate is given by the constitutive equation for Power Law creep, in the form,

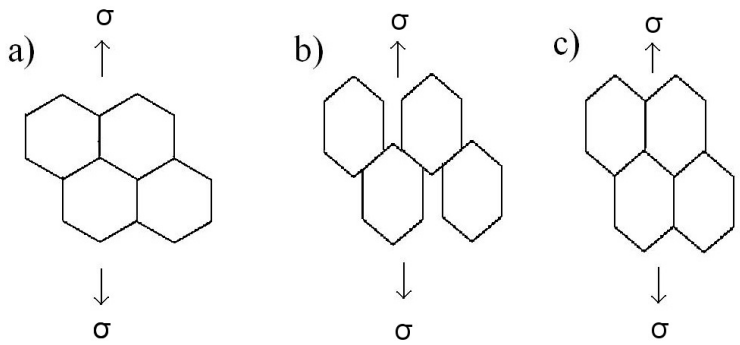

Figure 2.6. The grain boundary sliding process occurring in sequence. a) Grains before deformation, b) elongated grains following deformation, with internal voids if grain boundary sliding does not concur with creep, c) the grains following sliding and healing of potential internal voids. The slower of two rates is the dominating mechanism.

$$\dot{\epsilon} = A\sigma^n \exp(\frac{-Q}{kT}) \tag{2.15}$$

where A and n are properties of the specific creep mechanism. An equation representative of the constitutive equation for Power Law creep has been given by Wong et al [55] to study two different mechanisms. The total strain rate, as discussed above, is the sum of the individual mechanisms, with the greater rate giving the net creep rate. This is expressed in the form,

$$\dot{\epsilon}_{total} = \dot{\epsilon}_{PowerLaw} + \dot{\epsilon}_{Diffusion} = A_1\sigma^{n_1} \exp(\frac{-Q_1}{kT}) + A_2\sigma^{n_2} \exp(\frac{-Q_2}{kT}) \tag{2.16}$$

where the constants A_1, A_2, n1, and n2, are the coefficients and stress exponents which depend on the dominant creep mechanism. Changing the two stress exponents provides the ability to model regimes such as Nabarro-Herring and Coble creep ($n = 1$) at lower stresses, as well as power law creep at moderate stresses (n greater than 1), occurring simultaneously in a sample.

This model was developed by Wong et al [55], by combining and curve fitting 11 different sources of data on Pb/Sn eutectic solders. The model gives the steady state creep behavior with two regions with differing slopes on a plot of log stress versus log strain rate, where the slopes are equivalent to the stress exponents. This model has been shown to fit data from different sources. It has the capability of describing and separating the creep mechanisms occurring in conjunction with each other. This Double Power Law equation is not a standard form of the creep equation given in ANSYS, and therefore a user subroutine must be developed in order to study creep in regimes of mixed dominance. The development and implementation of the model will be discussed further in the next chapter.

CHAPTER 3

CREEP MEASUREMENTS OF HIGH TEMPERATURE MATERIALS

3.1 High Temperature Materials

In environments above $1500°C$ creep becomes a crucial design factor. High temperature applications are driving the need for a fundamental understanding of the creep resistance of high temperature materials (HTMs). These materials include refractory metals, platinum group metals, silicides, nitrides, borides and carbides. These materials are classified by their high melting temperatures, making them popular candidates for use in high temperature applications. Their material properties and applications will be discussed in this section.

Refractory metals are characterized by their extremely high melting temperatures. They are highly resistant to heat and wear. The metallic elements include zirconium (Zr), hafnium (Hf), niobium (Nb), tantalum (Ta), molybdenum (Mo), tungsten (W), rhenium (Re), ruthenium (Ru), osmium (Os), rhodium (Rh), titanium (Ti), and iridium (Ir). Refractory metals have high strength and hardness at high temperatures [21]. Furthermore, they have a low thermal expansion coefficient. The material properties of these refractory metals is included in Table 3.1, below.

The most widely used metallic elements are tungsten, molybdenum, tantalum and niobium. Tungsten has the highest melting point of all the elements. Tungsten is used in light bulb filaments, furnace wires, spark plugs, cutting tools and as an alloying agent in steel. Molybdenum is used for heat sinks, furnace fixtures for industrial heating, components in glass processing and as an alloying agent in steel. Tantalum

Table 3.1. Refractory metal properties [21].

Property	**Mo**	**W**	**Ta**	**Nb**	**Zr**	**Hf**
Melting Point ($°C$)	2,617	3,422	3,017	2,477	1,855	2,233
Thermal Expansion ($10^{-6}C^{-1}$)	4.8	4.5	6.3	7.3	5.7	5.9
Density (kg/m^3)	10,280	19,250	16,650	8,570	6,511	13,310
Young's Modulus (GPa)	329	411	186	105	68	78
Poisson's Ratio	0.31	0.28	0.34	0.40	0.34	0.37
Property	**Re**	**Ru**	**Os**	**Rh**	**Ir**	**Ti**
Melting Point ($°C$)	3,186	2,334	3,033	1,964	2,466	1,668
Thermal Expansion ($10^{-6}C^{-1}$)	6.2	6.4	5.1	8.2	6.4	8.6
Density (kg/m^3)	21,020	12,370	22,610	12,450	22,650	4,507
Young's Modulus (GPa)	463	447	560	275	528	115
Poisson's Ratio	0.30	0.30	0.25	0.26	0.26	0.32

is resistant to corrosion from acids, organic chemicals and aqueous solutions of salts. Due to these properties, tantalum is used for chemical resistant lining for reaction vessels and tubing. However, tantalum is vulnerable to hydrogen embrittlement. Niobium is used in superconductors, high temperature structural materials and also as an alloying agent in steel [33]. Refractory metals are alloyed for the improvement of low temperature ductility, creep resistance [41], oxidation resistance [50] and toughness [52].

The differentiation between refractory metals and platinum group metals (PGM) is subtle, and sometimes certain PMGs are classified as refractory group metals. Platinum group metals include platinum (Pt), palladium (Pd), ruthenium (Ru), osmium (Os), rhodium (Rh), and iridium (Ir). These metals form intermetallic compounds with aluminum (Al), scandium (Sc), vanadium (V), niobium (Nb), tantalum (Ta) and zirconium (Zr), which are good for high temperature structural applications. PMGs have high specific gravity with low specific strength and low specific moduli at high temperatures. Like the refractory metals, they have a high melting temperature. PMGs are used in applications in the aerospace and glass industries. In some applications, they have replaced nickel based superalloys that have a maximum service

temperature of 1100°C. Platinum group with intermetallic compounds are usually alloyed to improve creep resistance, ductility and strength [55, 36]. The material properties of PMGs are included in Table 3.2, below.

Table 3.2. Platinum group metal properties [55].

Compounds	**Melting Temperature** (°C)	**Specific Gravity** (g/cm^3)	**Compounds**	**Melting Temperature** (°C)	**Specific Gravity** (g/cm^3)
IrNb	1,900	15.25	Ir_3Zt	2,280	18.0
$Ru_{11}Ta_9$	2,080	14.41	Ir_3Ti	2,115	18.5
IrAl	2,120	-	Ir_3V	2,100	18.5
RuAl	2,060	7.97	Rh_3Ta	2,457	14.0
RuSc	2,200	7.40	Rh_3Nb	1,963	11.7
RuTi	2,120	8.55	Rh_3Zr	1,900	11.0
RhTi	1,940	8.5	Rh_3Ti	1,750	10.5
Ir_3Hf	2,470	< 20	Rh_3V	1,740	11.0
Ir_3Ta	2,454	< 20	Pt_3Al	1,556	-
Ir_3Nb	2,435	18.5	Pt_3Zr	2,154	18.0

Silicides are intermetallic compounds of silicon (Si) and Nb, Zr, Mo, or Ti. Silicides have an average melting temperature of 2000°C [37]. The advantage of silicides is the formation of an oxidation resistant layer of silica. This layer provides a protective coating for high temperature applications [50, 48]. Molybdenum disilicide ($MoSi_2$) has good oxidation and creep resistance, making it a great candidate for high temperature structural applications. Niobium silicide is another promising material for its application in jet engine turbine blades.

Ultra-high temperature ceramics (UHTCs), with melting points above 2700°C, include nitrides, carbides and borides, which are compounds of N, C and B, respectively. UHTCs are characterized the unique pairings of high melting temperatures and electrical conductivity, thermal shock resistance and chemical stability, and high strength and hardness. Furthermore, UHTCs have better resistance to oxidation and chemical change, lower density and higher strength than nickel superalloys. UHTCs

are well suited for high temperature applications including high temperature electrodes, molten metal crucibles and thermocouple sheaths. Improvements in shaping and machinability of these materials are being made through the use of organic lubricants and binders, or composites [4, 56].

Silicon nitride (Si_3N_4) and silicon carbide (SiC) and their composites have applications in land based propulsion systems [48]. These compounds can be used as substitutes for other metallic alloys. However, they are limited by brittleness and susceptibility to thermal shock [37].

3.2 Conventional Testing Methods

The potential applications for the previously mentioned high temperature materials have been discussed. However, before the using these HTMs it is necessary to determine their mechanical behavior, more specifically their creep deformation at high temperatures. Creep becomes an important design factor above half the melting temperature. Conventional methods of creep testing will be discussed in the following section.

Creep is conventionally measured with tensile and/or compression testing machines, as shown in Figure 3.1. An electric furnace is used for heating the sample. The top of the sample is attached to a fixture that must have equal or better mechanical and chemical properties at high temperatures. At elevated temperatures the sample becomes more reactive and it becomes increasingly more important that the sample not react with the fixture. A constant load is supplied by a weight fixed to the bottom of the sample. Conventional testing methods are limited to roughly $1700°C$, as shown in Table 3.3 [20, 10, 1, 3, 25, 28, 24, 18, 11, 32]. Researchers have conducted conventional creep tests on tungsten and its alloys up to $2100 - 2800°C$ [41, 19, 54], however under conditions which are not applicable to all materials. These experiments were carried out via heated wire specimens through electric resistance.

Table 3.3. Conventional creep tests

	Loading	**Heating method**	**Material**	**Temp.** $^{\circ}C$
Kinsey [27]	Uniaxial tension	Furnace	Metals, Alloys	1100
Allen et al. [1]	Uniaxial compression	Furnace	Ti, Zr, V, Nb, Ta, Cr, Mo, W, Pt, Pa, Rh, Ir, Fe, Co, Ni	1000
Johnson et al. [25]	Uniaxial compression	Furnace	Low carbon steel	700
Armstrong et al. [3]	Uniaxial tension	Furnace	Cermets	1400
Green [19]	Uniaxial tension	Self electrical resistance	W wire	2800
Wright [54]	Uniaxial tension	Self electrical resistance	W wire	2527
Endo et al. [18]	Uniaxial fatigue	Furnace	Cr-Mo-V, 304 Stainless Steel	600
Carroll et al. [11]	Uniaxial tension compression	Furnace	SiC	1300
Gundarev et al. [20]	Internal pressure	-	Mo-Zr-Nb-C tube	1550
Lindblom et al. [32]	Uniaxial tension	Furnace	Steels	1150
Jenkins [24]	Uniaxial tension	Furnace	SiC, Si_3N_4	1500
Kloc et al. [28]	Helicoid spring	Furnace	Fe, CuAl, NiCr, P-91	670
Park [41]	Uniaxial tension	Self electrical resistance	W-4Re-0.32HfC	2127
Buckman [10]	Uni/biaxial Loading	-	Nb, Ta, Mo based alloys	1500

Non-conductive materials, as well as materials that cannot be formed into wires cannot by tested using this method. High temperature creep behavior is frequently extrapolated from measurements at low temperatures. The extrapolation is often inaccurate, demonstrating the limitations of conventional creep testing in providing useful information for high temperature applications.

Figure 3.1. Conventional high temperature creep testing machines for ceramics.

For these reasons, a new method of creep testing is required to study materials above $2000°C$. An understanding of the creep behavior of UHTMs for high efficiency energy conversion systems, aerospace power systems, thermal and electric rockets and hypersonic jet engines is in high demand. Non-contact creep testing methods will be discussed in the following section, as a new method for testing above $2000°C$.

3.3 Containerless Testing Methods

Due to the limitations of conventional creep tests, non-contact testing methods involving levitation of the sample are necessary to test HTMs. Levitation testing

methods for creep measurements include the use magnetic forces and electrostatic forces. A review of the applications, advantages and drawbacks of various levitation methods will be discussed in this section.

Electromagnetic levitation (EML) is used to levitate spherical samples and measure the deformation of a rotating sample. A magnetic field is generated by a coil, which produces levitation forces. The sample is placed inside of the coil, where magnetic induction creates eddy currents. With enough eddy currents a Lorentz force is generated that is capable of levitating the sample [9]. This method is only applicable to conductive materials.

Since the 1960s EML has been used to measure density [49, 51, 16], thermal expansion [13, 14], surface tension [5, 15], electrical resistivity [34] and viscosity of molten and liquid metals [15, 34]. The first non-contact measurement of creep was demonstrated by Kiessig, et al, using EML in vacuum [26]. Heavier samples require larger levitation forces which are attainable through increased power to generate higher eddy currents [42]. However, with increased power comes to ability to overheat or melt the sample. Further drawbacks include the contamination from the blown gas used to control the temperature of the sample.

In electrostatic levitation (ESL), levitation of the spherical sample is achieved through electrostatic forces. The sample is placed between two vertical electrodes with a static charge [46, 43, 45]. A deuterium arc lamp supplies the sample with high energy photons which causes the expulsion of electrons. Now, the positively charged sample is levitated in the electric field between the anode and cathode. A feedback system controls the horizontal position of the sample through three pairs of orthogonal electrodes in the horizontal plane [9, 45]. A heating laser controls the temperature, allowing the tests to be done in vacuum [45]. Furthermore, the heating laser allows ease in changing the temperature. ESL is particularly advantageous because the heating of the sample is independent of rotation. Additionally, contami-

nation by atmospheric gases and large temperature gradients are eliminated with the use of vacuum in ESL. This method can be applied to conductive and non-conductive materials. ESL has been used in the measurement of density [19, 7], viscosity, surface tension [45, 22, 23, 44] and electrical conductivity.

Other techniques have been shown to levitate samples, but have not yet been used for measuring creep. These methods include acoustic and aerodynamic levitation through the use of high power speakers and gas jets, respectively. The acoustic levitation method is used for the determination of material properties of molten materials in both stable and metastable states [9]. Aerodynamic levitation has been used to measure electrical conductivity [17, 47], permeability [33] and density [40].

3.3.1 Experiment and Apparatus

ESL methods have been used to measure the creep deformation behavior of niobium at temperatures as high as $2300°C$ [30]. The measurement method is founded on a rotating sphere experiencing a shear stress that depends on the angular velocity, ω, the radius r, and the density of the sample, ρ. The maximum shear stress of a rotating sphere is given by,

$$\tau(\omega) = 0.211\omega^2 r^2 \rho \tag{3.1}$$

The applied load causes the sample to creep. Currently, stresses as high as 100 MPa in the center of the sphere have been reached, and by rotating the sample even faster the stress can be further increased. The stress scales with the square of the angular velocity, providing large gains in stress with increasing angular velocity.

Non-contact creep measurements were conducted at the NASA Marshall Space Flight Facility (MSFC) in Huntsville, AL, using the ESL apparatus, as seen in Figure 3.2. The sample was levitated via Coulomb forces, under vacuum in an electrostatic

field. The sample was rotated using photon pressure, with a laser pointed off center in the horizontal plane.

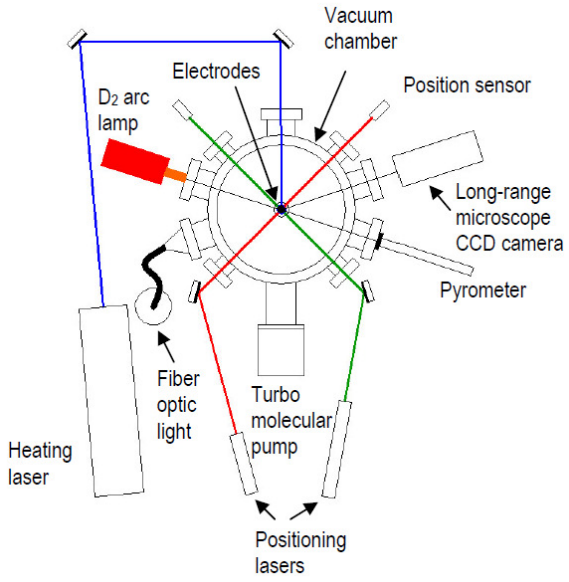

Figure 3.2. Schematic of the MSFC ESL facility and the optical measuring tools [29].

More recently, experiments have been carried out with rotation of the sample caused by an induction motor instead of photon pressure. Hyers and coworkers, in collaboration with NASA MSFC developed an electromagnetic induction drive to decouple stress from the temperature of the sample, providing more flexibility in non-contact creep measurements. An induction drive was used to rotate a cold sample from rest to a specified rotation speed. The sample is placed in a rotating magnetic field, which induces a current to give torque. The torque is proportional to the square of the magnetic field. Alternating current from two pairs of coils mounted 90° apart, is driven 90° out-of-phase, resulting in a magnetic field of uniform intensity that rotates with the frequency of the applied current. A proportional torque is given by the difference in speed between the rotation of the magnetic field and the sample.

A rotation device based on a rotating magnetic field was developed and constructed at UMass. The device was installed in NASA MSFC's ESL apparatus and tested with samples of 316 stainless steel. Samples of other materials, including ZrB_2, a SiC and ZrB_2 composite, and Ni and Nb based superalloys, have been accelerated from rest to over 33,000 revolutions per second driven via the induction motor.

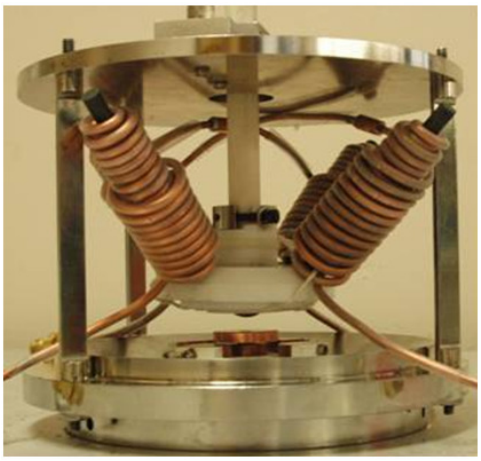

Figure 3.3. Induction motor design developed in the previous work.

Deformation of the sample was recorded with a digital camera, every 30 minutes before deformation began, and then every 10 minutes thereafter. Edges of the sample were detected using machine vision software developed in the previous work at UMass [8]. The ESL creep test was validated by conventional creep tests carried out at the University of Tennessee [31]. Previous research using ESL reported a stress exponent of 2.482 ± 0.002, which is in good agreement with the value of 2.4 ± 1 determined via conventional creep measurement on high purity niobium.

3.3.2 The Stress Exponent and Experimental Parameters

It was found that the polar and equatorial radii varied as a function of time. Furthermore, a stress distribution, varying with distance from the sample center, was observed to exist. It was hypothesized that the stress exponent determines the

deformation of the sample, and thus could be determined directly from the deformed shape. A series of finite element analyses using different stress exponents confirmed this prediction.

The time-resolved deformation behavior is defined by fitting images with sixth-order Legendre polynomials to the edge of the deformed sample. The radius at a specific latitude, given by $r(\theta)$, is shown below with constants a_i, and latitude θ .

$$r(\theta) = \sum_{i=0}^{6} a_i P_i \left[cos(\theta)\right] \tag{3.2}$$

The previous work fit Legendre polynomials to the detected edge of the deformed spheres from experiments. A function relating the edge to the rotation angle was determined. In the current work, a Legendre polynomial fit is found for the deformed spheres generated by the FEA models. The unknown coefficients are determined by requiring that the Legendre series match the numerical solution at the boundary. That is, the Legendre series fits to the edge of the deformed sample by finding the unknown coefficients.

3.3.3 Advantages of the Containerless Methods

ESL has many advantages over conventional creep testing methods. ESL testing can be done in vacuum, unlike the acoustic and aerodynamic testing methods. The ESL method allows for heating of the sample in vacuum via a heating laser. Heating by laser provides easy control of the sample temperature. Conducting experiments in vacuum is advantageous due to the lack of contamination by cooling or atmospheric gases. Furthermore, there are no large temperature gradients in the sample.

There are additional benefits supplied by conducting ESL tests in vacuum. Theoretically there is no upper limit on temperature for ESL tests. Moreover, ESL methods avoid contamination of the sample through contact. Smaller samples are needed to conduct measurements, giving the method advantages in cost and availability of new

materials for the sample. Furthermore, as a result of the variation of stress as a function of the radius, the stress exponent can be determined in a single test, as opposed to the conventional method requiring multiple tests. Thus, the method provides both a reduction in time and cost. Finally, the measurement of the stress exponent exhibits high precision, with an approximate error of $\pm 0.6\%$ for stress exponents between 2 and 5. Accuracy can be increased through using high-precision spherical samples and taking measurements at larger strains.

While the previously used ESL method holds advantages over the conventional methods for testing creep, it suffers the limitation of coupling between temperature and acceleration rate of the sample due to rotation by photon pressure from the heating laser. Use of the electromagnetic induction drive provides a method to decouple the temperature of the sample from the acceleration rate, and thus the loading rate. Therefore, the electromagnetic induction extends the experimental temperature range for high stresses. Furthermore, it allows low temperature tests to be conducted and compared to results from conventional tests at the same temperature.

CHAPTER 4

SIMULATIONS OF NON-CONTACT CREEP

FEA has proven to be an effective method for modeling creep behavior for various materials including metals, ceramics, composites, mortar and solids. The numerical analysis of this research was carried out using the FEA software ANSYS. The purpose of this analysis is to reduce the computation time of the previous analyses and determine what the creep deformation measurements should look like in regimes of mixed dominance.

4.1 Three-Dimensional Norton creep

Previous numerical modeling was conducted by Hyers and coworkers using 3-D model of the creep deformation of the sphere in ANSYS. While a rotating sphere is axisymmetric, permitting 2-D finite element modeling, a 3-D model was developed to study the sensitivity to the depth of scribe [29]. A deep scribe is made on the surface of the sample to facilitate counting the number of rotations. FEA studies were performed to determine the appropriate depth of the scribe to allow axisymmetric deformation while maintaining a large enough scribe to determine the rotation rate. For the other purposes of study, including validation of experimental results, and the identification of the correlation between the deformed shape of the sample and the stress exponent, a 2-D model is appropriate, if not preferred. The 3-D model of the creep deformation of the rotating sphere will be outlined in this section, as well as the validation of the model. The models developed in the current research are built upon the framework of the 3-D model, and will be validated against results from this model.

The Norton creep model was selected as the constitutive equation of steady state creep in this analysis, due to its ability to model power law creep and its programming-friendly representation. The basic mathematical model is given by,

$$\dot{\epsilon} = A\sigma^n \exp(\frac{-Q}{kT}) \tag{4.1}$$

where A is a material constant, σ is the applied stress, n is the stress exponent, Q is the activation energy for creep at elevated temperatures, k is Boltzmann's constant and T is the temperature.

For the 3-D finite element analysis, Solid186 was chosen to model the sphere for its prediction of creep deformation, as noted in the ANSYS user's manual [53]. Solid186 is a higher order 3-D element that demonstrates quadratic deformation behavior, and is well suited for plasticity, hyperelasticity, creep, large deflection and strain. The 10-noded tetrahedral option was selected, allowing quadratic deformation, and is shown below [29].

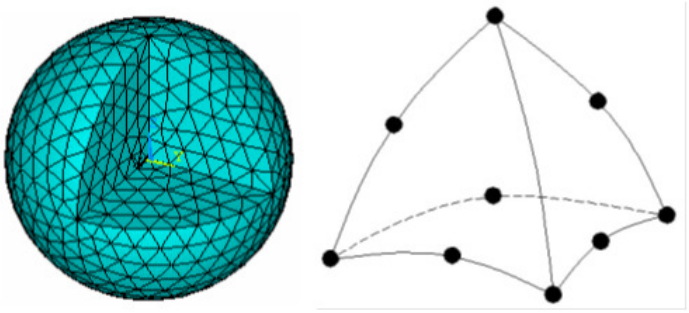

Figure 4.1. Sphere (with an eighth removed) on the left, and the 10-noded tetrahedral option on the right.

The meshed model shown in Figure 4.1 has 4,995 elements and 7,602 nodes. The degrees of freedom in the x-y plane were constrained in the vertical direction. The degrees of freedom for nodes on the z-axis were constrained in the horizontal direction.

The displacement of the node at the center of the sphere is prevented in all three directions.

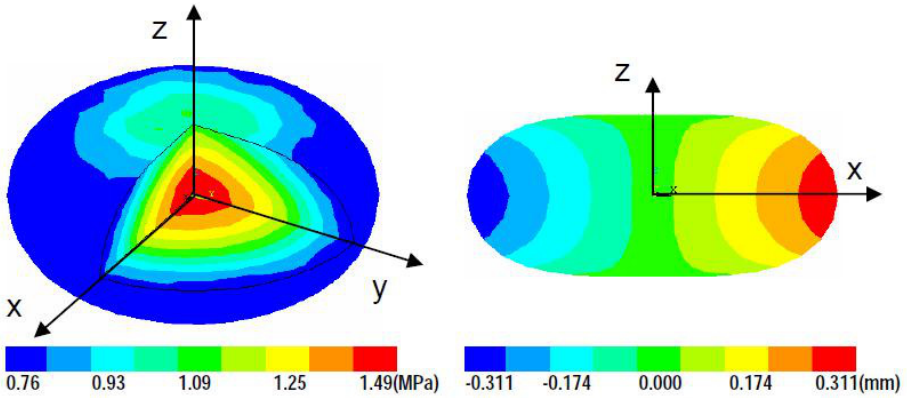

Figure 4.2. von Mises stresses developed due to the centripetal acceleration (left), and the displacement in the x-direction (right) at 3,600 seconds. [29]

Lee reported fair agreement between the experimental and numerical results from the 3-D Norton model for the creep deformation of the rotating sphere [29]. Therefore, the FEA developed previously was validated for future use. The new models of the creep deformation of the rotating sphere will be validated initially in comparison with the existing model for 3-D Norton creep.

4.2 Two-Dimensional Norton Creep

4.2.1 Motivation

Since the deformation of the sphere is axisymmetric, and as well as mirror symmetric about the equatorial plane, it can be modeled in two dimensions. The previous model was used as a framework for creating the 2-D model. Changing the deformation model from 3-D to 2-D is beneficial for its greatly reduced computation time. Taking full advantage of the axisymmetry of the deformation, as well as the mirror symmetry, allows a model of just a quarter circle of the vertical cross section of the

sphere, as shown in the figure below. A mesh size of 0.0001 m for a 1mm diameter sphere is then cut from 45,216 nodes to just 343 nodes for the quarter circle. Simulations previously requiring approximately 5 hours can now be completed on the order of minutes on a quad-core Intel i7 2.8GHz.

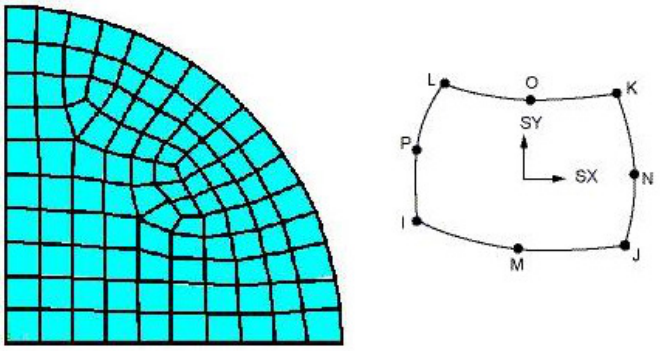

Figure 4.3. Quarter circle with meshsize 0.0001 m (left), and Plane183 8-noded element (right).

4.2.2 Model Specifications

A quarter of the cross-sectional area of the sphere is created in 2-D. The meshing of the quarter circle is shown in Figure 4.3. The Plane183 element was selected to model the 2-D cross-section of the sphere. Plane183 is a higher order 2-D element with quadratic displacement behavior, and works well for irregular meshes, as indicated in the ANSYS user's manual [53]. Furthermore, Plane183 is appropriate for plasticity, hyperplasticity, creep, large deflections and strains. The axisymmetric option for Plane183 was activated. The 8-noded quadrilateral element, shown in Figure 4.3, was selected.

Appropriate boundary conditions were applied to prevent the model from translational motion. Nodes on the y-axis were constrained in the horizontal direction, and nodes on the x-axis were fixed in the vertical direction, thus allowing deformation of the sphere while fixing the origin in space.

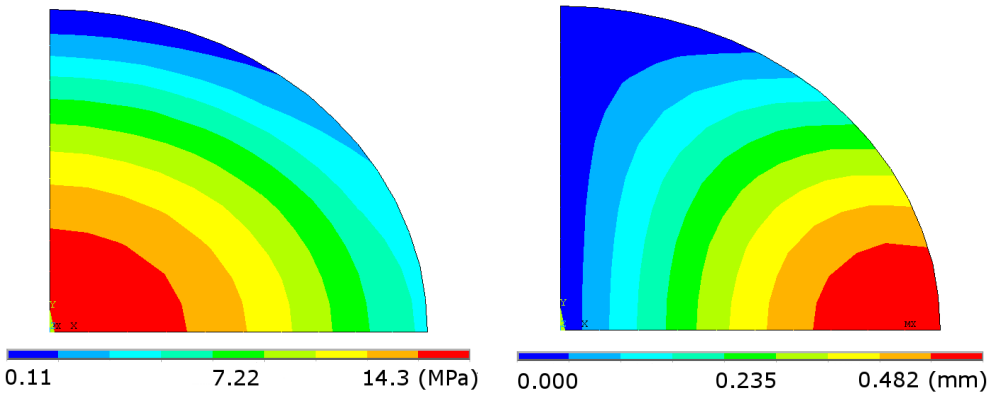

Figure 4.4. Left, von Mises stress and right, x-displacement for deformed sphere of pure niobium with $n = 1$ at 10,000s.

4.2.3 Validation of the Model

A perfectly spherical sample was assumed with a 1 mm radius. Furthermore, isotropic material properties were assumed for pure niobium. The modulus of elasticity, Poisson's ratio and density were set to 1.03 x 10^{11} Pa, 0.38 and 8562 kg/m^3, respectively [35]. The temperature of the sample was assumed constant at 2258°C, which is $0.9T_m$, as seen in the denominator of Equation 2.15. The stress exponent was set to 4, to model Power law creep. The constant was set to 5 x 10^{-23} MPa^{-4} s^{-1}, which encompasses the exponential term, $\exp(-Q/kT)$, as the temperature was assumed constant. The constant was chosen for a 1 mm radius sphere run up to an equatorial strain of 0.09. Simulations were carried out to 2000 seconds at maximum shear stresses of 1.68, 3, 5, and 7 MPa using both the 2-D and the 3-D Norton creep models. The values for equatorial and polar displacements for each model are shown in Table 4.1.

The polar and equatorial displacements from the 3-D and 2-D models are found to be in good agreement with each other with a maximum relative percent error of less than 0.002%. The 2-D Norton model will be used for future research.

Table 4.1. Equatorial displacements from 2-D and 3-D Norton creep FEA models.

Stress (MPa)	**3D Norton Equatorial Displacement** (mm)	**2D Norton Equatorial Displacement** (mm)	**Relative percent error**
1.68	0.00003950611850	0.00003950611840	0.00000025%
3	0.00027302596300	0.00027303740000	0.00418897%
5	0.00195850173000	0.00195839583000	0.00540719%
7	0.00760766092000	0.00760883336200	0.01541133%

4.3 Two-Dimensional Double Power Law Model

4.3.1 Motivation

To study the creep deformation behavior in regimes of mixed dominance, a model addressing multiple mechanisms is required. The double power law creep model as discussed previously will be used to model simultaneous creep mechanisms. The 2-D Norton creep FEA model will be used as the basis for this model, but the Norton constitutive equation for creep will be replaced with the following equation,

$$\dot{\epsilon}_{total} = A_1\sigma^{n_1}\exp(\frac{-Q_1}{kT}) + A_2\sigma^{n_2}\exp(\frac{-Q_2}{kT}) \tag{4.2}$$

where the constants $A_1, A_2,\ n_1,$ and $n_2,$ are the coefficients and stress exponents which depend on the dominant creep mechanism. This equation allows for multiple mechanisms to take place at once. The user can select stress exponents to represent several different creep mechanisms, such as Nabarro-Herring, Coble or various Power Law creep stress exponents. The dominating creep mechanism is determined by the given combination of applied stress and temperature.

4.3.2 Model Specifications and Subroutine

ANSYS provides thirteen built-in creep functions, with equations including Norton and Strain-Hardening, among others. However, the built in functions do not include a constitutive equation representative of the Double Power Law creep model.

Therefore, the development of a subroutine was required to study regimes of mixed dominance. One of the user programmable features (UPFs) for the user creep equation was implemented. A user-defined creep law was developed using the usercreep.F subroutine. ANSYS recommends the use of usercreep.F as opposed to usercr.F because it is implicit, giving efficient, robust and accurate results, as noted in the ANSYS user's manual [53]. A usercreep.F, written in Fortran 90, file is provided by ANSYS that models the first built creep equation, the strain-hardening law. This file may be manipulated to serve the purposes desired by the user, and was used as a foundation for this research.

Inputs for the creep subroutine generally are written in the creep strain rate form and depend on stress and temperature, fitting well within the desired model for this research. The output of the subroutine must include `delcr`, the incremental creep strain rate. Additionally, the derivatives of incremental effective creep strain with respect to stress and the creep strain, `dcrda(1)` and `dcrda(2)` respectively, must also be passed back to ANSYS.

The subroutine is given five inputs by the user, including A_1, A_2, n_1, n_2, and Q/k. Materials properties and geometric specifications are prescribed in the same text file, and are fed into ANSYS. The subroutine calculates the derivative of the incremental creep strain with respect to the stress, and the value is passed back to ANSYS. The subroutine allows for any combination of coefficients and stress exponents to simulate the deformation behavior in regimes of one or two dominant mechanisms.

4.3.3 Validations of the Model

Simulations using the Double Power Law model were carried out to compare results with the other two models in an effort to validate the model. The same material properties from Section 4.2.3 were assumed for a perfectly spherical sample with a 1 mm radius. First a set of simulations was carried out to compare the 2-D

Norton model to the 2-D double power law model as a means for a rapid evaluation. Following the comparison of these two models, simulations of the Double Power law model were carried out to measure the error between both the 3-D and 2-D Norton models. These sets of simulations will be explained in further detail in this section.

In the double power law model, when one of the coefficients is set equal to zero the equation becomes identical to the Norton equation for creep,

$$\dot{\epsilon}_{total} = A_1\sigma^{n1}\exp(\frac{-Q_1}{kT}) + 0\sigma^{n2}\exp(\frac{-Q_2}{kT}) \Rightarrow (A_1\sigma^{n1})\exp(\frac{-Q_1}{kT}) \tag{4.3}$$

allowing exact comparison of the two models. For a stress exponent equal to 6, various simulations were run using the 2-D Norton and 2-D double power law model with one of the coefficients set equal to zero. The simulations were run for A_1 set to zero, and then the case with A_2 equal to zero to ensure the model's full functionality. Simulations were carried out to 2000, 3000 and 5000 seconds at maximum shear stresses of 1.68, 3, 5, and 7 MPa using both the 2-D and the 3-D Norton creep models. The models give exact agreement with each other out to the 9th decimal place, for both equatorial and polar displacements.

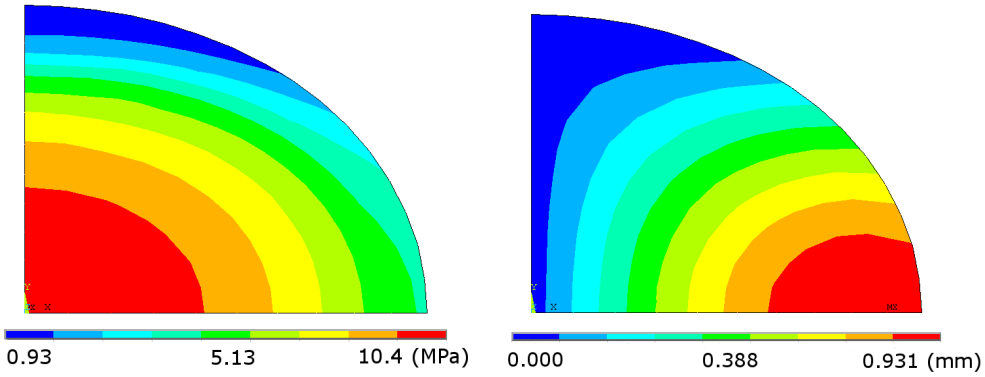

Figure 4.5. Left, von Mises stress and right, x-displacement for deformed sphere of pure niobium with $n_1 = 1$ and $n_2 = 4$ at 15,850s.

4.3.4 Comparison of the Models

Simulations with the DPL model were carried out to compare the results to the 3-D and 2-D Norton models that were discussed in the previous sections. The same material properties and temperature were kept in place. Simulations with a stress exponent of 4 were carried out to 2000 seconds at shear stresses of 1.68, 3, 5, and 7 MPa. Again, the equatorial displacements of the 2-D Norton and DPL models were in exact agreement to the 9th decimal place. The percent error between the 2-D and 3-D models is under 0.02% for each of the cases.

Table 4.2. Equatorial displacements for each model, and percent error.

Stress (MPa)	**3D Norton Equatorial Displacement** (mm)	**2D Norton percent error**	**2D DPL percent error**
1.68	0.00003950611850	0.00000025%	0.00000025%
3	0.00027302596300	0.00418897%	0.00418897%
5	0.00195850173000	0.00540719%	0.00540719%
7	0.00760766092000	0.01541133%	0.01541133%

The 2-D models, including the Norton and Double Power Law constitutive equations, show excellent agreement with the 3-D Norton creep model developed in the previous work. The 2-D Norton and 2-D Double Power Law models will be used for future research. The determination of creep measurements in regimes of mixed dominance will be studied using the Double Power Law model developed in this work.

4.4 Validation with Experimental Results

To further validate the Double Power Law model, numerical results were compared to experimental data taken over a region of transition between dominating mechanisms. Experimental data from Harper and Dorn's work in 1957 [38] was used. A plot of the stress versus strain rate from the experiment is shown in Figure 4.6. The

details of the test geometry are unknown, except that a tensile test was performed, as discussed in Section 3.2.

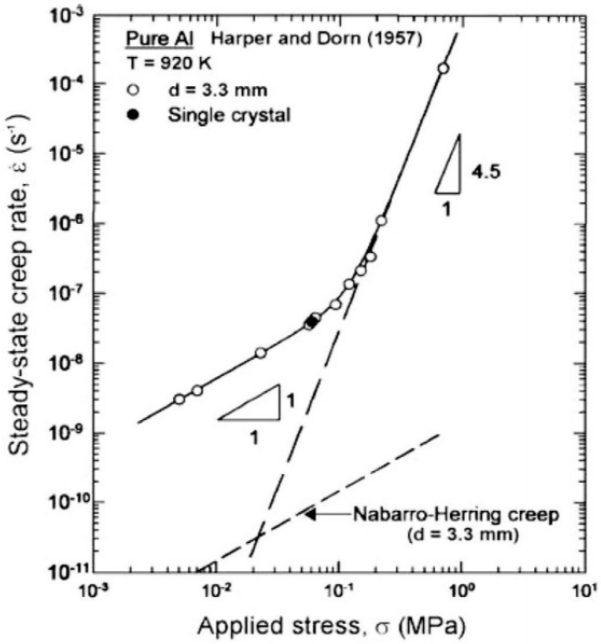

Figure 4.6. Harper and Dorn results [38].

Harper and Dorn conducted experiments on high purity aluminum at $0.99T_m$ and found polycrystalline aluminum showed many diffusional creep properties, but gave a much larger strain rate than expected. The strain rate was proportional to the stress, but much was faster than they had expected for Nabarro-Herring creep. The same strain rate relation was found for single crystals as well. They found that at higher stresses the strain rate increased roughly with the fourth power of the applied stress, and was indicative of dislocation creep.

The numerical models from the current work were compared to the experimental creep results of high purity aluminum at a high temperature. The experimental work found a stress exponent of 1 and 4.5, with a transition at an intermediate stress, as shown in Figure 4.6. The numerical simulations in the current work used stress exponents of 1 and 4.5. The temperature of the sample was set to 920K, as it was in

the experiment. Simulations were carried out over a range of stresses to capture the region of transition between diffusional and dislocation creep.

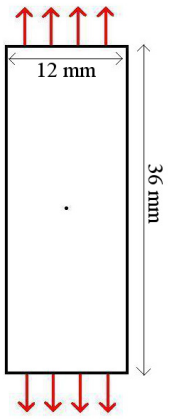

Figure 4.7. The basic geometry of the rectangle used in numerical simulations. Rectangle was placed in vertical tension, with constant load indicated by red arrows.

A simple 2-D rectangle with a height of 36mm and width of 12mm was placed in vertical tension, as shown in Figure 4.7. A constant load was applied on either end of the rectangle, as indicated in the figure. First, simulations using the 2-D Norton FEA model were carried out. The results from simulations with a stress exponent of 1, and other simulations with a stress exponent of 4.5, are illustrated in Figure 4.8. Coefficients of 8 x 10^{23} MPa^{-1} s^{-1} and 3 x 10^{2} $MPa^{-4.5}$ s^{-1}, were used with stress exponents of 1 and 4.5, respectively.

The results from the 2-D Norton model with n=1 are in excellent agreement with the experimental results in low stress region. In this region the stress versus strain rate curve is linear indicating that the dominating mechanism is solely due to diffusional creep. In the higher stress region, simulations with a stress exponent of 4.5 using the 2-D Norton model give creep rates that are in great agreement with the experimental results.

Simulations using the 2-D Double Power Law model were carried out to examine the creep behavior in the region of transition between n = 1 and n = 4.5. The

numerical results are plotted with the experimental results and are shown in Figure 4.8. The model gives results that are in good agreement with experimental results taken in regimes of mixed dominance, as well as the two ends of the stress range.

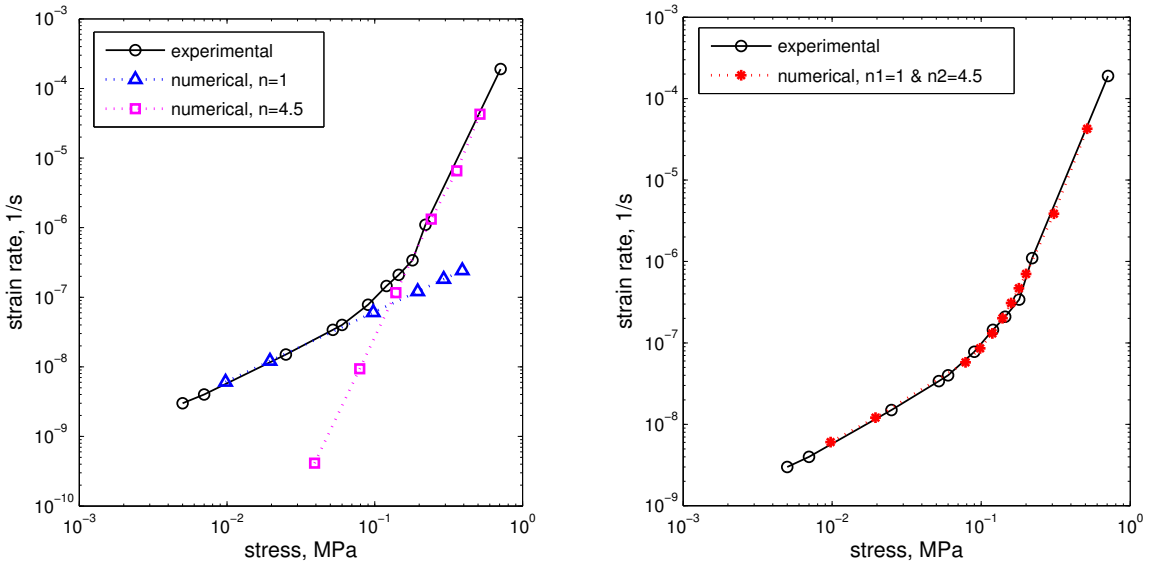

Figure 4.8. Comparison of numerical results to experimental data for the rectangle in tension. Left, single mechanism results using the 2-D Norton creep model. Right, results of double mechanism creep from the 2-D Double Power Law model.

The same process described above for the rectangle in tension, was carried out with simulations of a rotating 1mm radius sphere of pure aluminum. The numerical simulations in the current work used stress exponents of 1 and 4.5, with the same coefficients as before. The maximum stress developed at the center of the rotating sphere was taken, with the corresponding strain rate near the center of the sphere. These local strain rates for the sphere over a range of stresses are illustrated in Figure 4.9. Again, the results from the 2-D Norton model for single mechanism creep are shown on the right, and the 2-D Double Power Law results are shown on the left. The results from both models are in excellent agreement with the experimental results of Harper and Dorn.

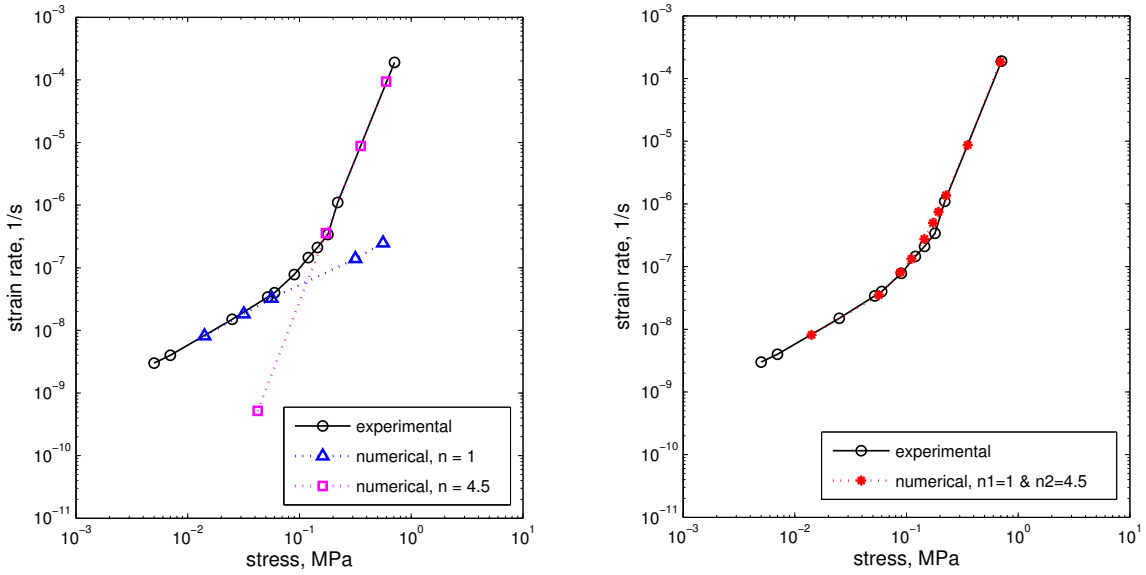

Figure 4.9. Comparison of numerical results to experimental data for the rotating sphere. Left, single mechanism results using the 2-D Norton creep model. Right, results of double mechanism creep from the 2-D Double Power Law model.

The Double Power Law model has been validated against previous FEA models of the deformation of a rotating sphere. Furthermore, the Double Power Law model has been validated by comparison with experimental results in a region of transition between dominating mechanisms for both a rectangle in tension and a rotating sphere. The results from the model show good agreement with experimental data. This model will be used for future research.

CHAPTER 5

CHARACTERIZATIONS OF REGIMES OF MIXED CREEP DOMINANCE

The goal of this work is to identify the cases in which transitioning mechanisms change the surface shape of the sample. The difference in surface shapes due to multiple dominating mechanisms must be characterized. The FEA models were used to simulate and then quantify the differences in the creep behavior for single versus double mechanism creep. There are various ways to examine the effect of transitioning mechanisms on the shape of the in a sample. These include studying the stress versus strain rate, the apparent stress exponent over a range of stresses, radius ratio and finally, Legendre polynomial curve fitting of the shape of the deformed sphere. These methods and analyses will be discussed in this chapter. This work examines the effect of regimes of mixed creep dominance on the precision of the measurement using non-contact testing methods.

Table 5.1. Stress exponent combinations studied in this work. Diffusional creep is expected to dominate at low stresses and Power Law creep at high stresses.

n_1	**Mechanism**	n_2	**Mechanism**
1	Diffusion	4	Power Law
1	Diffusion	5	Power Law
1	Diffusion	6	Power Law

Simulations were carried out over a range of stresses to study the relationship between the deformation of the sample and the stress exponent for both single and double mechanism creep. Various combinations of stress exponents were examined,

with initial simulations focused on combinations of $n_1 = 1$ and $n_2 = 4$, 5, and 6, from Equation 2.16. Table 5.1 displays the combinations of stress exponents and the corresponding mechanisms that were studied in this work. Diffusional creep, such as Nabarro-Herring and Coble, should dominate at low stresses, while Power Law creep should dominate at higher stresses. This work focuses on the intermediate region of stress in which multiple mechanisms are dominant. The pre-exponential constant A was chosen so that the range of strain rates fell within the the range of stresses being investigated.

5.1 Stress Versus Strain Rate

5.1.1 Motivation

Multiple creep mechanisms can be active in a sample, however they dominate in different regimes depending on stress, temperature and grain size. The point of transition from one mechanism to another was determined by running simulations of single mechanism creep over a range of stresses. Further simulations using the Double Power Law model exhibited the discrepancy in strain rates for the two models at the same stress. Comparison between results from the single and double mechanism models allows a quantified approach in identifying the region of transition. This section describes the simulations and analyses that were carried out to characterize the differences in strain rates for single versus double mechanism creep. Furthermore, the relationship between stress and strain rate in regions of creep mechanism transition illuminates the effect on measurements and the degree of necessity in avoiding experimentation in those regions.

5.1.2 Simulations and Analysis

First, simulations of single mechanism creep were carried out using the 2-D Norton creep model discussed in the previous chapter. Each combination of two stress expo-

nents was first simulated as individual stress exponents to model single mechanism creep.

Simulations were run to a final strain criterion of 0.09. The strain rate at the termination of the simulation was taken. The von Mises stresses were recorded from the center of the deformed sphere. The Von Mises, or equivalent stress, is a measure of the stress intensity, and is given by,

$$\sigma_{von\,Mises} = \sqrt{\frac{(\sigma_1 - \sigma_2)^2 + (\sigma_1 - \sigma_3)^2 + (\sigma_2 - \sigma_3)^2}{2}} \tag{5.1}$$

where the subscripts 1, 2 and 3 indicate the axes of the corresponding normal stresses.

All simulations were carried out assuming a perfect sphere of pure niobium. The material properties listed in Section 4.2.3 were used again for these simulations. The temperature of the sample was assumed constant at $2258.15°C$. Results were compiled on a log-log plot of the stress versus strain rate. A linear relationship for each single mechanism simulation was found, as expected, with the slope of each line equal to the respective single mechanism stress exponent. This expected results follows from taking the log of each side of the Norton creep equation, resulting in the following equation,

$$\dot{\epsilon} = A\,\sigma^n \exp(\frac{-Q}{kt}) \tag{5.2}$$

$$ln(\dot{\epsilon}) = ln\left[(A\ \exp(\frac{-Q}{kt})\sigma^n)\right] \tag{5.3}$$

$$\Rightarrow ln\left[(A\ \exp(\frac{-Q}{kt}))\right] + ln(\sigma^n) \Rightarrow ln\left[(A\ \exp(\frac{-Q}{kt}))\right] + n\,ln(\sigma) \tag{5.4}$$

where $ln\left[(A\ \exp(\frac{-Q}{kt}))\right]$ is a constant that gives the y-intercept, n is the slope and $ln(\sigma)$ is the variable on the x-axis. Simulations were carried out over a range of stresses that was large enough to capture the intersection of the two single mechanism curves. The region encompassing the intersection of curves is of greatest interest in this work,

as it is the area in which the creep mechanism transitions, and should be modeled using the Double Power Law model.

Upon completion of the 2-D Norton creep simulations, deformation behavior of double mechanism creep was studied. These simulations were carried using the 2-D Double Power Law model discussed in the previous chapter. The two stress exponents in the DPL model were set equal to the individual stress exponents used in the single mechanism studies. Again, simulations were conducted over a range of stresses, with an emphasis on the region of transitioning mechanisms. A greater number of simulations were conducted inside the region of transition.

The stress in the rotating sphere varies continuously throughout the sample. The stress varies from a maximum value in the center of the sphere to zero at different locations. The stress value reported in this work is the maximum stress, located in the center of the sphere.

The stress versus the strain rate from the single and double mechanism simulations were plotted on a log-log scale to provide comparison of the deformation behavior. The difference between single mechanism creep and the transitioning regions of double mechanism creep can be quantified in terms of strain rate over a range of stresses. It was expected that the Double Power Law model would produce results in which the log of the strain rate would be linear with respect to the log of the stress in low stress and high stress regions. In some intermediate range of stresses, where the two single mechanism lines interest, it was expected that the double mechanism results will deviate from the single mechanism curves. These expectations were met, and are shown in Figures 5.1 - 5.3. The discrepancy between single and double mechanism results was quantified in an effort to characterize the deformation in regions of transitioning mechanisms, as well as the effect of the transition on the precision of the experimental measurement. This will be discussed further in the results section.

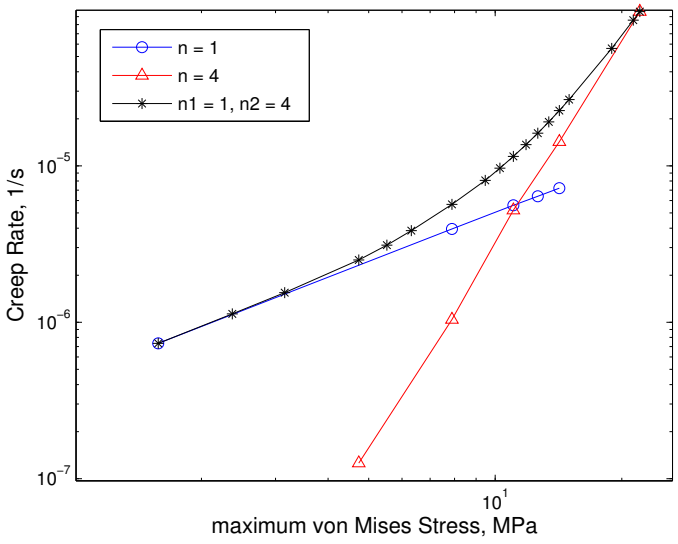

Figure 5.1. Single mechanism vs. Double mechanism results for creep strain as a function of stress for n = 1 and n = 4, and the combination of the two stress exponents.

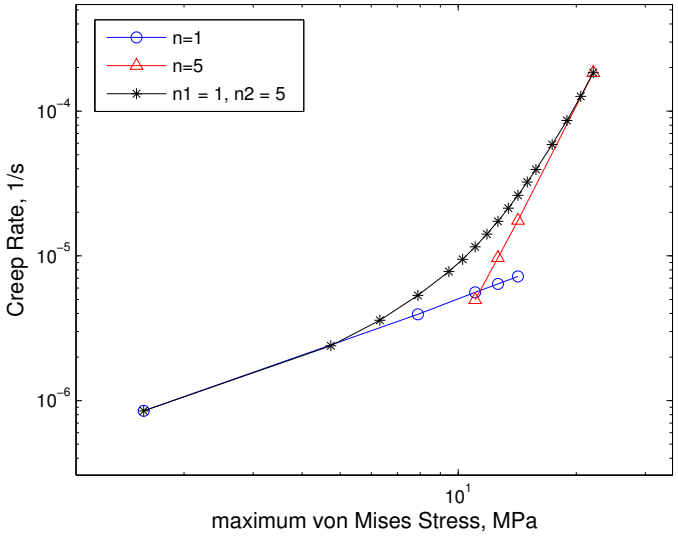

Figure 5.2. Single mechanism vs. Double mechanism results for creep strain as a function of stress for n = 1 and n = 5, and the combination of the two stress exponents.

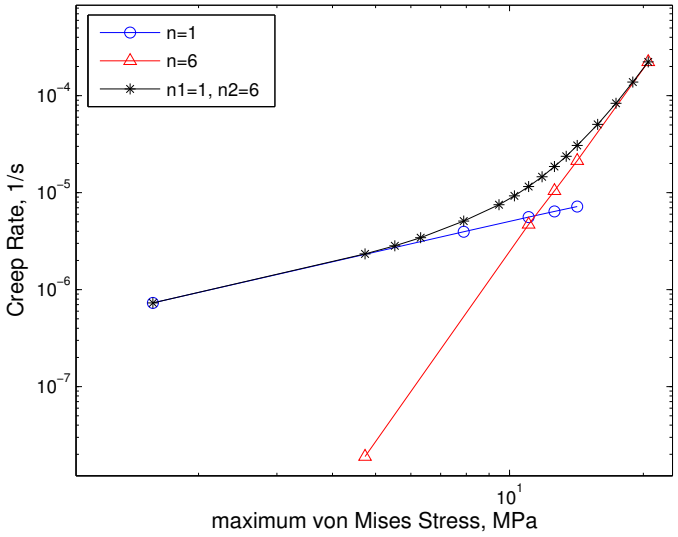

Figure 5.3. Single mechanism vs. Double mechanism results for creep strain as a function of stress for n = 1 and n = 6, and the combination of the two stress exponents.

5.1.3 Results

Shown in Figures 5.1 - 5.3 are plots of the stress versus strain rate on a log-log scale. The stress versus strain rate curve for diffusional creep with n = 1 is shown in blue circles. Power law creep is displayed with red triangles, with stress exponents of 4, 5 and 6. Finally, the black asterisks exhibit the stress strain-rate relationship for simulations using the Double Power Law creep model. The plots illustrated that the Double Power Law model is in good agreement with the diffusional creep rate at low stresses, and with the Power Law creep rate at high stresses, with an independent creep rate at intermediate stresses.

The percent error between the strain rate for single versus double mechanism creep was quantified using the following equation,

$$percent\ error = (\frac{strain\ rate_{single} - strain\ rate_{double}}{strain\ rate_{single}})x100\% \qquad (5.5)$$

Where the single mechanism strain rate was taken at the intersection between the two independent mechanisms, and the double mechanism strain rate was taken at the stress at which the independent mechanisms intersected. This allows the calculation of the maximum difference between strain rates from the two models. The difference between the two curves is shown schematically with the arrow in Figure 5.4. The percent errors were found to be -105.3229%, -106.1788% and -107.0364% for n = 1 and 4, 5 and 6, respectively. The maximum difference between strain rates from single versus double mechanism creep models exceeds 105% for each of the cases discussed in this work. The precision of the strain rate measurement is therefore greatly affected in regimes of mixed dominance.

It is clear that the deformation of the sphere in the region of transition is not in exact agreement with the strain rates of the single mechanism creep model. The Double Power Law model, in the window of transition, gives a creep rate that is independent of the single mechanism models for each of the cases studied, with a maximum difference greater than 105%.

5.2 Equatorial and Polar Radii

5.2.1 Motivation

Additionally, the polar and equatorial radii for single and double mechanism simulations were studied. The difference in radii between the two models was quantified in an effort to characterize the effect of transitioning regions on the deformation of the sample. The radius ratio will be calculated as the ratio of the equatorial radius to the polar radius, as shown in Figure 5.5. Previous work demonstrated that the radius ratio decreased monotonically with increasing stress exponent. This work examined how the regime of mixed dominance fits within this scheme. The change in the radius of the sample in regimes of mixed dominance was studied, and the results are included

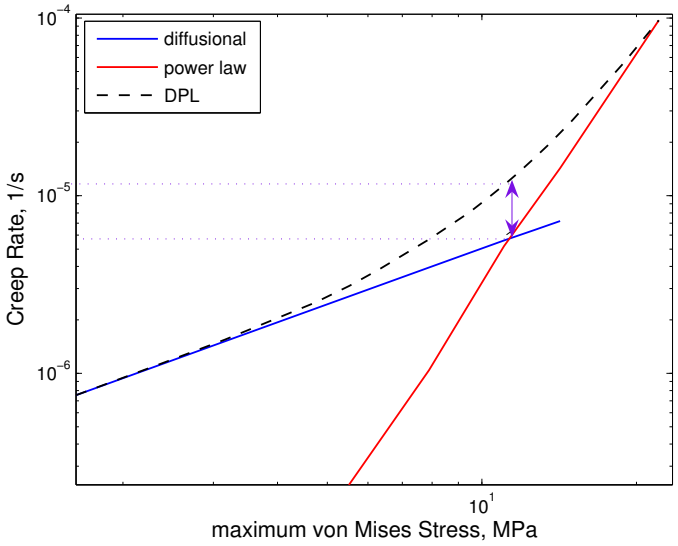

Figure 5.4. Schematic of strain rate versus stress curves to demonstrate where the relative errors between single and double mechanism creep results were calculated. Difference is represented by purple arrow. The maximum difference between strain rates for each of the three combination of stress exponents studied, exceeded 105%.

in this section. The goal of this analysis is to look at the effect of double mechanisms on the precision of the creep measurement.

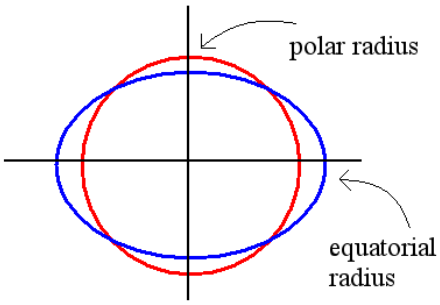

Figure 5.5. Schematic of the polar and equatorial radii. Original shape of the sample is shown in red, deformed sample is represented in blue.

5.2.2 Simulations and Analysis

Simulations of perfectly spherical samples of pure niobium were carried out to an equatorial strain criterion of 0.11. The transient simulations were carried out with a coarse time step, until the equatorial displacement surpassed 94% of the desired strain, when a finer time step was used for the remainder of the simulation. The simulations were stopped when the given strain criterion was reached. Single mechanism creep was simulated with the 2-D Norton model. Regimes of mixed creep dominance were simulated with the Double Power Law model. Again, simluations were carried out in regions where double mechanism creep plays a role in the deformation of the sphere. The ratio of equatorial to polar radii was calculated over the range of stresses. Additionally, the transience of the radii was examined across the range of stresses. Single mechanism results from the 2-D Norton model were compared to double mechanisms results from the Double Power Law model, and are discussed further in the next section.

5.2.3 Results

The radius ratio across the range of stresses which encompass the region of mechanism transition are shown in Figures 5.6 - 5.8. Again, it was found that the radius ratio decreased monotonically with increasing stress exponent. In each figure diffusional creep is shown in blue, Power Law Creep in red and Double Power Law is shown in black. It was illustrated that the radius ratio for Double Power Law creep varies linearly between the bounds given by diffusional and Power Law creep. In the low stress region, the radius ratios of diffusional and Double Power Law creep are in good agreement with each other, confirming that diffusional creep is the dominating creep mechanism at low stresses. In the higher stress region the Double Power Law radius ratio tends towards the radius ratio for Power Law creep.

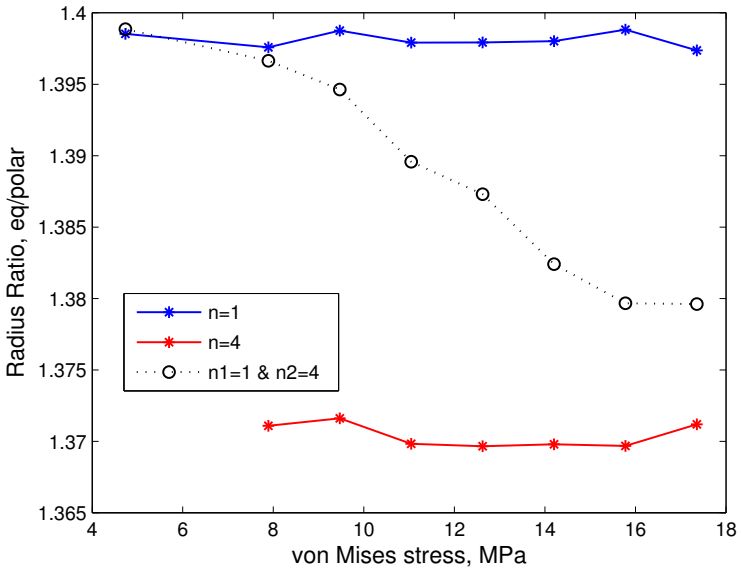

Figure 5.6. Variation in the Radius Ratio with stress, for n = 1 and n = 4, and the combination of the two stress exponents.

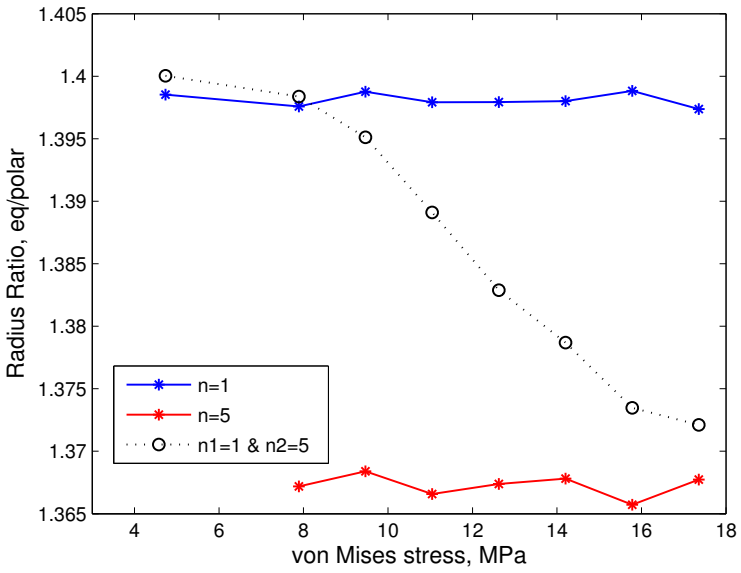

Figure 5.7. Variation in the Radius Ratio with stress, for n = 1 and n = 5, and the combination of the two stress exponents..

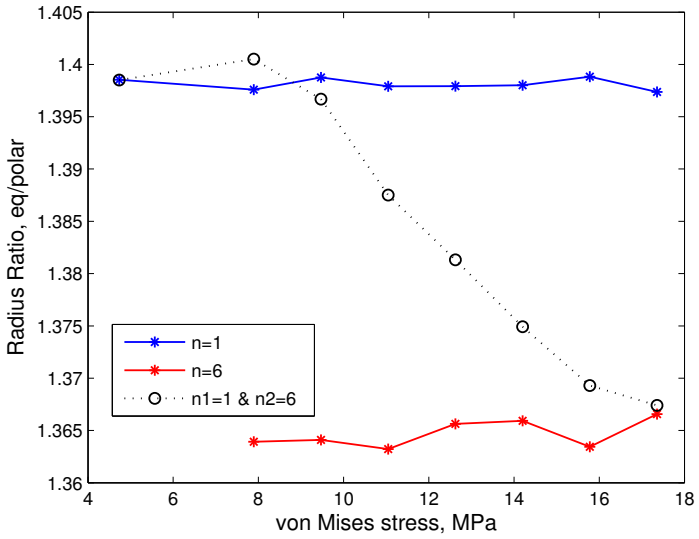

Figure 5.8. Variation in the Radius Ratio with stress, for n = 1 and n = 6, and the combination of the two stress exponents..

The difference in polar radii between single and double mechanism creep was quantified using the following equation.

$$percent\ error_{polar} = \left| \left(\frac{polar\ radius_{single} - polar\ radius_{double}}{polar\ radius_{single}} \right) \right| x100\% \qquad (5.6)$$

Figure 5.9 exhibits the absolute value of the percent error between the polar radii of diffusional creep and Double Power law creep, displayed in blue. In red, the percent difference between Power Law and Double Power Law creep is shown. The percent difference varies linearly between the two ends of the stress range.

5.3 Apparent Stress Exponent

5.3.1 Motivation

It was shown in the previous section that the slope of the strain rate curve for double mechanism creep varied between the two slopes of the individual single mechanism

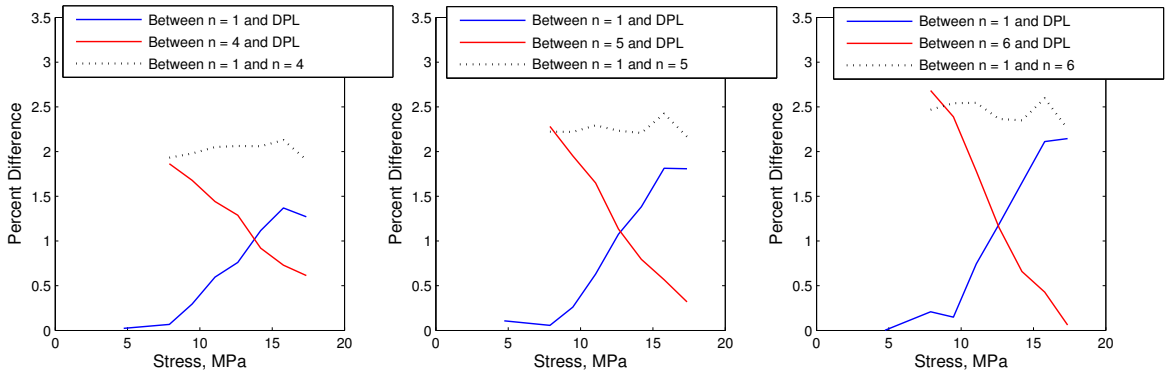

Figure 5.9. Difference in radius ratio.

creep results. That is, at low stresses the slope of the double mechanism creep curve was in agreement with results for single mechanism creep with n = 1, and at higher stresses the slope matched that of the single mechanism power law creep. In these ends of the stress range the double mechanism results are in such good agreement with the single mechanism results, that if these values were to be found experimentally, it would be assumed a single mechanism was dominating in the sample. Furthermore, the stress exponent for that dominating mechanism would be easily deduced from the slope of the curve.

However, if data from the region of transition were found experimentally, what stress exponent would be assumed? If experimental results are obtained from the regime of mixed dominance, but a single dominating mechanism is assumed, an apparent stress exponent would be determined, instead of the correct combination of two independent stress exponents. This work studies the apparent stress exponent in the region of transitioning mechanisms.

5.3.2 Simulation and Analysis

Results from Section 5.2, on the radius ratio of deformed samples with a final equatorial strain criterion of 0.11, provide the basis for this study of the apparent

stress exponent. The radius ratio for individual data points are taken from the Double Power Law results. These radius ratios are compared to results from single mechanism simulations with the same material properties, maximum stress and strain criteria. Further sets of simulations were carried out for single mechanism creep to determine the stress exponent for single mechanism creep that produces the same radius ratio found from the double mechanism model. These single mechanism simulations were carried out for comparison with the radius ratio data collected for n = 1 and n = 5, and the combination of those two stress exponents.

5.3.3 Results

Simulations of single mechanism creep were carried out for nine data points across the range of stresses. At each stress, a different stress exponent was found to provide agreement in radius ratios between the single and double mechanism results. The radius ratios for the double mechanism results, of n = 1 and 5, are illustrated by black circles in Figure 5.10. The single mechanism results are shown in magenta triangles, demonstrating the agreement of radius ratios. Each of the single mechanism data points shown in magenta have a unique stress exponent, that is apparent stress exponent. The value of the apparent stress exponent across the range of stresses is shown in Figure 5.11.

The apparent stress exponent values, found by the radius ratio comparison method, vary across the range of stresses as shown in Figure 5.11. The apparent stress exponent remains bounded by n = 1 at the bottom end, and n = 5 at the upper end. This demonstrates that across the range of stresses for which the dominating creep mechanism undergoes a transition, the apparent stress exponent varies monotonically between the two single mechanism stress exponents as expected.

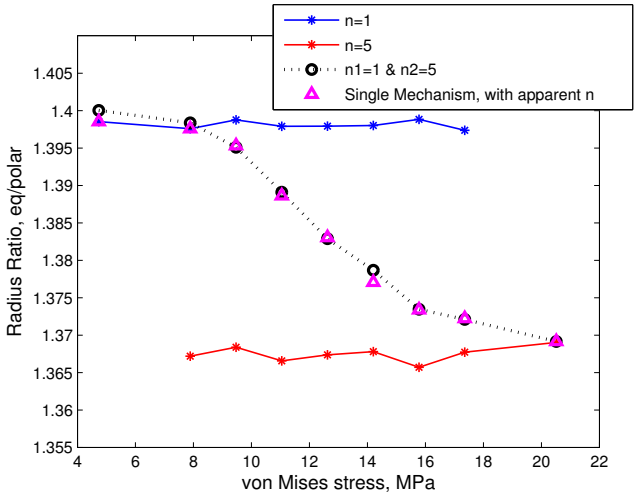

Figure 5.10. Radius ratio versus stress results for n = 1, n = 5 and combinations of the two stress exponents. In magenta triangles, the radius ratios for single mechanism cases with apparent stress exponents are shown to demonstrate the agreement in radius ratio.

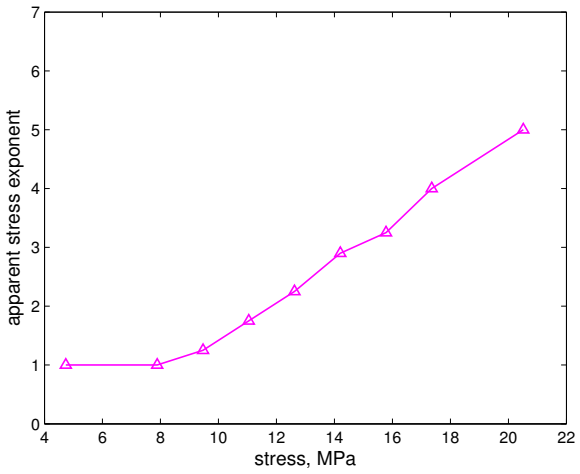

Figure 5.11. Apparent stress exponents found by the radius ratio comparison method.

5.4 Legendre Polynomial Curve Fitting

5.4.1 Motivation

An additional method to quantify and characterize the regimes of transitioning mechanisms is through the use of Legendre polynomial fitting as discussed briefly in

Chapter 2. A Legendre polynomial is a family of orthogonal polynomials defined on the interval $[-1, 1]$. Orthogonal polynomials are used in the theory and practice of function interpolation and approximation. In this research the Legendre polynomials are used for solving a boundary value problem. The Legendre series must match the solution at the boundary by determining coefficients that satisfy that requirement. That is, coefficients were found by demanding that Legendre series fit to the edge of the deformed sample. Furthermore, this work used Legendre polynomials in spherical coordinates to represent a function that depends on angles.

Previous work used Legendre polynomials in the image capturing scheme to determine the edge and shape of the deformed sphere from experiments. This work used the same mathematics in an effort to compare the deformation of single versus double mechanism creep found in numerical simulations. The sixth order Legendre polynomial is shown below.

$$r(\theta) = \sum_{i=0}^{6} b_i P_i \left[cos(\theta)\right] \tag{5.7}$$

which can be rewritten in the form,

$$r(\theta) = a_0 + a_1 cos(\theta) + a_2 cos^2(\theta) + ... + a_6 cos^6(\theta) \tag{5.8}$$

The goal of using Legendre polynomial curve fitting is to study the change in the coefficients, a_i, for varying creep mechanism simulations carried out to the same equatorial strain over a range of stresses. The Legendre polynomial curve fitting will be used to quantify the difference in the shape of the deformed sphere that depends on the dominating creep mechanism.

5.4.2 Simulations and Analysis

Simulations were carried out to a final equatorial strain of 0.09 over the same range of stresses that were studied in previous sections. The final x and y-displacements

at each node on the exterior of the sphere were output. These displacements were combined with the original node locations, respectively, to determine the final node location in x and y-coordinates. These coordinates were plotted to display the final silhouette of the deformed sphere, and is shown in Figure 5.12. This figure exhibits that in each of the three creep mechanism cases, the same equatorial strain was reached, however a unique polar strain was found for each case. It was proven that the shape of the deformed sphere varies with the dominating stress mechanism. The shapes of the deformed samples over a range of stresses in which transitioning mechanisms occur were plotted in an effort to identify and characterize the cases in which changing mechanisms play an important role in the creep behavior of the sample.

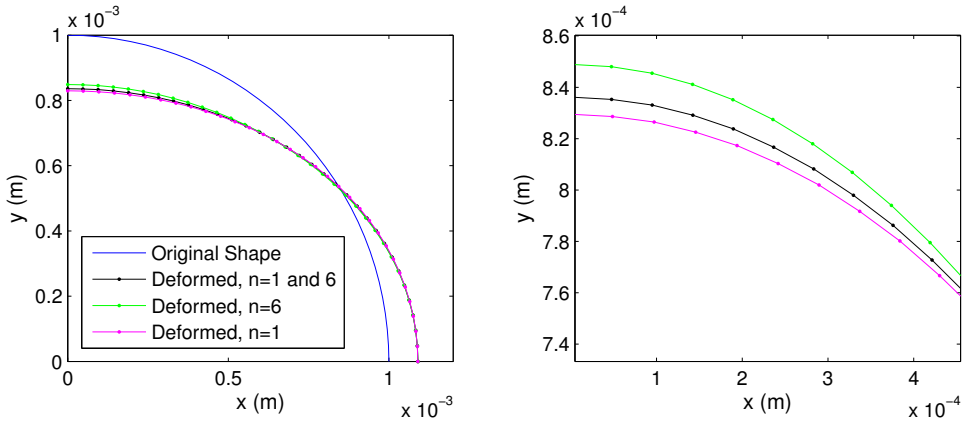

Figure 5.12. Left, Edge of the undeformed and deformed sphere, under varying stress mechanisms with combinations of n = 1 and n = 6, at a stress of approximately 17.5 MPa. Right, close-up of the polar radii for the three cases of simulations. It is illustrated that for the same equatorial strain, each stress exponent gives a unique polar strain.

The Cartesian coordinates of the edge of the deformed sphere were converted into polar coordinates to facilitate fitting of the Legendre polynomial of the form given in Equation 5.7. A least squares fit routine was implemented to fit the Legendre polynomial to the edge of the deformed sphere.

5.4.3 Results for One Quadrant of the Sphere

The FEA models give results for the deformation of the sphere in a single quadrant, as a by product of modeling the rotating sphere as axisymmetric. Initially, a least squares fit routine was used for a Legendre polynomial with only even terms, as shown in Equation 5.9. While the curve fitting provided very promising R^2 values, summary plots of the coefficients, a_i, for single and double mechanism deformation results did not demonstrate any sort of discernible trend across the range of stresses. In an effort to find a significant trend in the coefficients, fitting was carried out using both odd and even terms of the Legendre polynomial, as shown in Equation 5.10. Again, the trends in coefficients over the range of stresses provided no general pattern. As a final effort to identify a pattern in the coefficient values, the a_1 term was removed from the Legendre polynomial, as shown in Equation 5.11. The a_1 should provide an unwanted displacement instead of a deformation, as noted in Arfken [2]. The three Legendre polynomials are shown below in Equations 5.9 - 5.11, beginning with only even terms, then all terms, and finally omitting only the a_1 term.

$$r(\theta) = a_0 + a_2 cos^2(\theta) + a_4 cos^4(\theta) + a_6 cos^6(\theta) \tag{5.9}$$

$$r(\theta) = a_0 + a_1 cos(\theta) + a_2 cos^2(\theta) + a_3 cos^3(\theta) + ... + a_6 cos^6(\theta) \tag{5.10}$$

$$r(\theta) = a_0 + a_2 cos^2(\theta) + a_3 cos^3(\theta) + a_4 cos^4(\theta) + ... + a_6 cos^6(\theta) \tag{5.11}$$

A plot of the R^2 values for the least square fits to the Legendre polynomials is shown in Figure 5.13. It is demonstrated that across a range of stresses, the Legendre polynomial with all terms except for a_1 gives a consistently constant value of R^2, which is also closest to one. While the Legendre polynomials including only even terms, as well as all the terms, produce R^2 values close to one, they show greater fluctuation across the range of stresses.

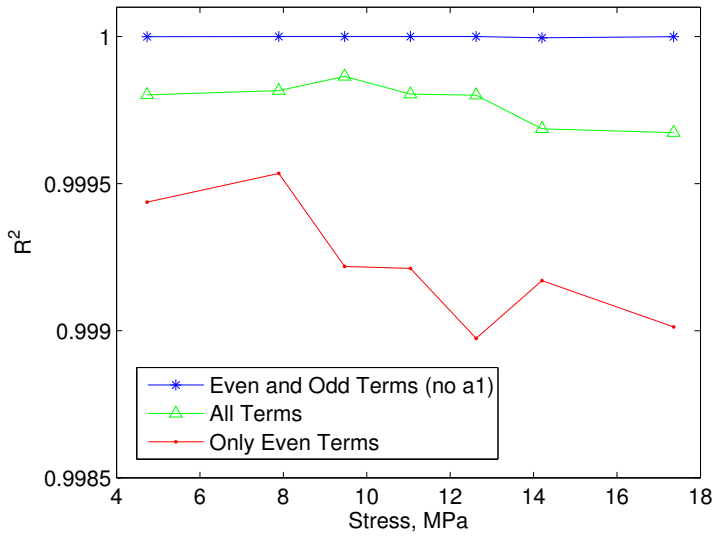

Figure 5.13. Making the case for all terms except a_1. These are from curve fitting n1 = 1 and n2 = 5 simulations with the Double Power Law Model to one quarter of the sphere. The Legendre series used for these fits are given by Equations 5.11-5.13.

Finally, Figure 5.14 displays the trends in the coefficients across the range of stresses. In each case of a_0 through a_6, excluding a_1, general patterns are better conveyed with the Legendre polynomial fits using all of the terms except the a_1 term. These patterns, along with the strong R^2 values, provide compelling evidence that the least-squares Legendre polynomial curve fitting should be done with all terms except a_1, as given by Equation 5.11.

Simulations were carried out over a range of stresses for each of the combinations of stress exponents shown in Table 5.1. The results are shown in Figure 5.15 , diffusional creep coefficients are presented in blue circles, Power law creep coefficients are given with red triangles, with stress exponents of 5, and the black asterisks represent the Double Power Law creep coefficients. A plot of each coefficient, a_i, is presented to demonstrate the trend in relation to the dominating mechanism.

Is it shown that that coefficients from the single mechanism deformation curve fits remain constant across the range of stresses. The deformation from the Double

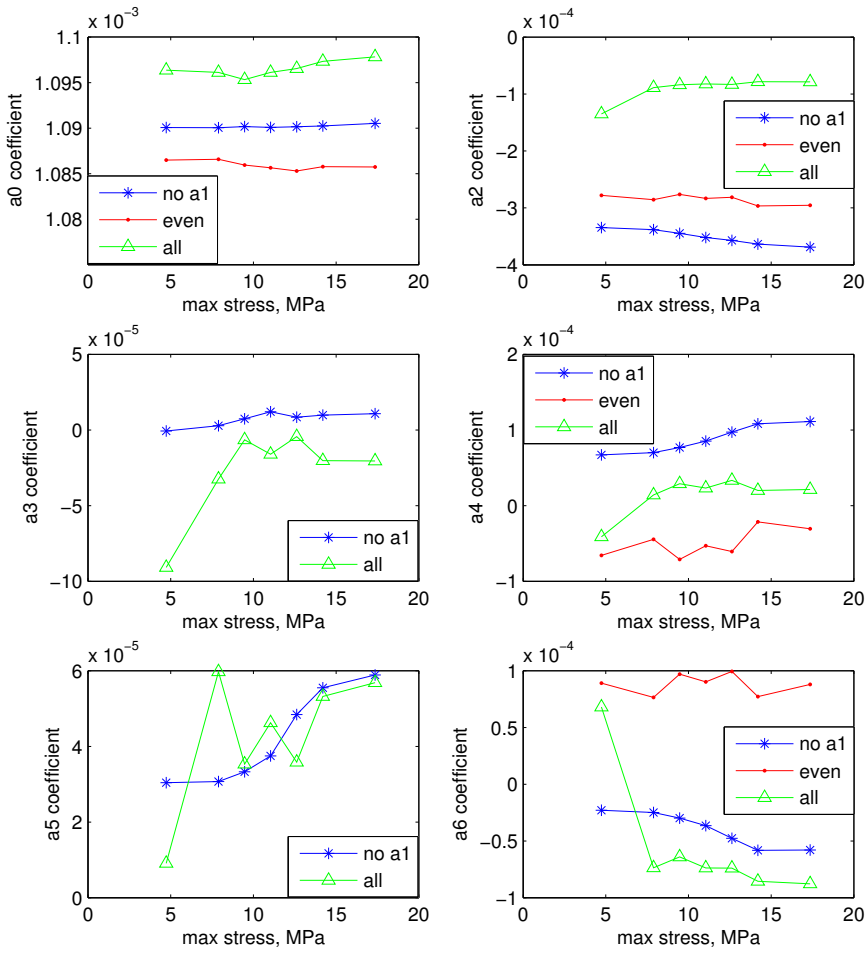

Figure 5.14. Legendre polynomial coefficients across a range of stresses for Double Power Law simulations of n1 = 1 and n2 = 5, fit to one quarter of the sphere. Green triangles show coefficients from fitting the deformed sphere with only even terms of the Legendre polynomial. Red dots show the coefficient found using all terms of the Legendre polynomial. Blue asterisks display the coefficients from the Legendre polynomial with all terms except a_1. The mechanism transition range is between 8-18 MPa, as shown in Figure 5.7.

Power Law model demonstrate that in regimes of mixed dominance many of the coefficients vary between the bounds of the corresponding single mechanism creep. The a_0 coefficient corresponds to the equatorial radius. Although a_0 appears to fluctuate

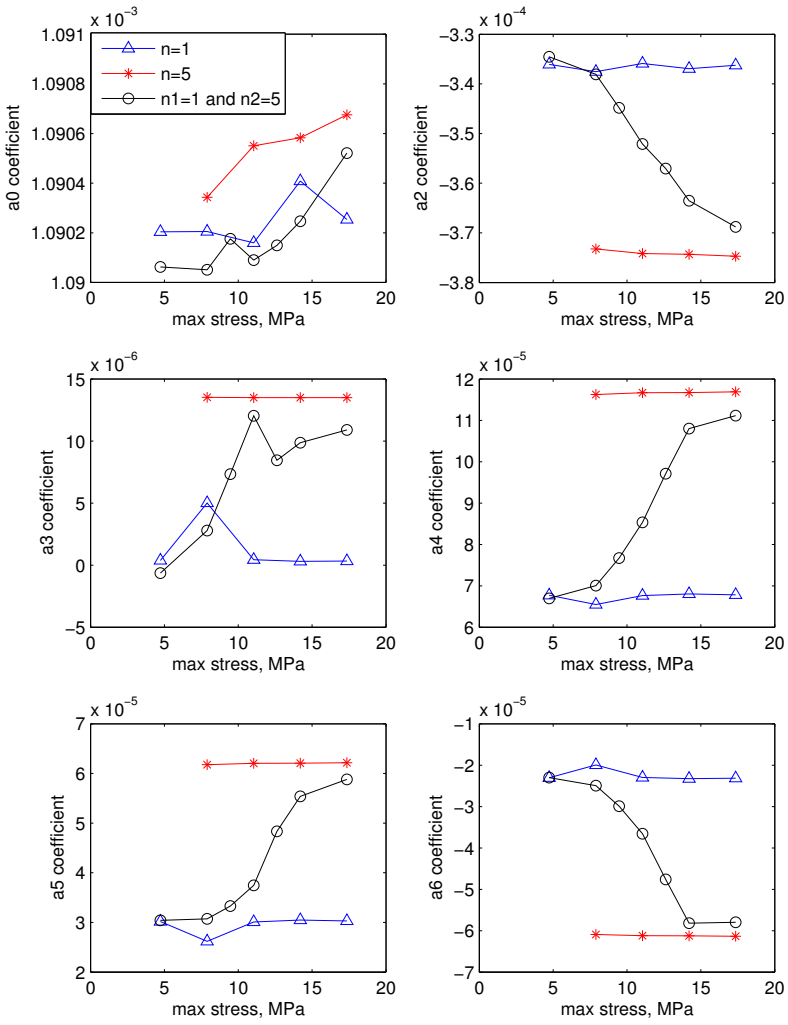

Figure 5.15. Legendre polynomial coefficients from curve fitting the edge of one quarter of the deformed sphere. Results from simulations of of n = 1 and 5 are shown here. The mechanism transition range is between 8 and upwards of 18 MPa, as shown in Figure 5.7.

across the range of stresses, it should be noted that the amplitude of fluctuation is extremely small.

Many of the other coefficients follow a generally linear trend between the bounds of the single mechanism coefficients. The region in which the coefficient varies between

the two bounds corresponds to the regime of mixed dominance. That is, the stress range in which the dominating mechanism is transitioning from diffusional to Power Law creep. The value of a_3 fluctuates in a manner that is inconsistent between simulations with different combinations of stress exponents. There appears to be no distinct pattern in the a_3 coefficient across the range of stresses. However, the other coefficients in the Legendre series do present a marked pattern. The magnitude of a_2, a_4, a_5 and a_6 all grow with increasing stress.

Previous discussion of the Legendre polynomial fits was based on the comparison of Legendre series with matching highest order terms. Analyses were also carried out to compare the quality of the fit for series with the same number of terms. The three Legendre polynomials with the same number of terms are shown below. Again the three series consist of one series with only even terms, one with all terms, and finally all terms except a_1.

$$r(\theta) = a_0 + a_2 cos^2(\theta) + a_4 cos^4(\theta) + ... + a_1 2 cos^{12}(\theta) \tag{5.12}$$

$$r(\theta) = a_0 + a_1 cos(\theta) + a_2 cos^2(\theta) + a_3 cos^3(\theta) + ... + a_7 cos^7(\theta) \tag{5.13}$$

$$r(\theta) = a_0 + a_2 cos^2(\theta) + a_3 cos^3(\theta) + a_4 cos^4(\theta) + ... + a_6 cos^6(\theta) \tag{5.14}$$

The coefficient of determination, or R^2 values, are shown in Figure 5.16. The R^2 values for both the series with only even terms and for all terms omitting a_1 are very close to one, signaling an excellent fit to the numerically generated data. The fit using all terms gives R^2 that fluctuate greatly across the range of stresses. From the perspective of the coefficient of determination, both equation 5.12 and 5.14 provide excellent models for the shape of the deformed sphere.

As before, the coefficients of the Legendre polynomials were plotted across the range of stresses in an effort to identify a pattern in the results. The coefficients for the Legendre polynomial fits for combinations of n = 1 and 5 are shown in Figure

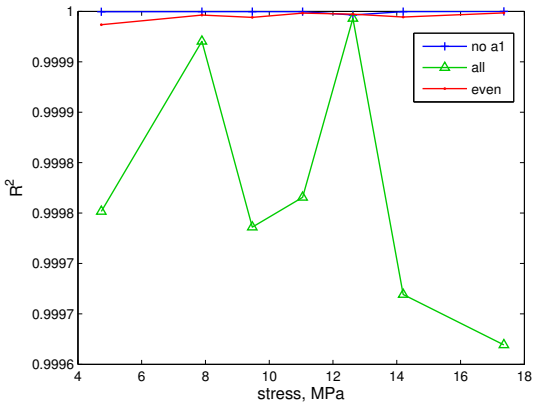

Figure 5.16. Making the case for all terms except a_1. These are from curve fitting n1 = 1 and n2 = 5 simulations with the Double Power Law Model. The Legendre series used for these fits are given by Equations 5.12-5.14.

5.17. As before, the patterns in the Legendre polynomial coefficients across the range of stresses are most pronounced for the series with all the terms except for a_1.

Finally, Figure 5.18 illustrates the patterns in the the a_i coefficients across the range of stresses for combinations of n = 1 and 5. The general trends are very similar to those found using six terms, and omitting a_1, as displayed in Figure 5.15. The coefficients a_2, a_4, a_5 and a_7 now should the most pronounced pattern.

Three Legendre series were compared with the same highest order term, and another set of three Legendre series with the same number of terms were compared. For each case, it was shown that omission of the a_1 term returns the most distinct trends in coefficients across the range of stresses. When comparing the Legendre polynomial curve fits from terms with the same highest order term, it was clear that omitting the a_1 term gave the best R^2. This was not the case with the comparison of Legendre series with the same number of terms, but omitting the a_1 term continued to provide excellent fits to the data.

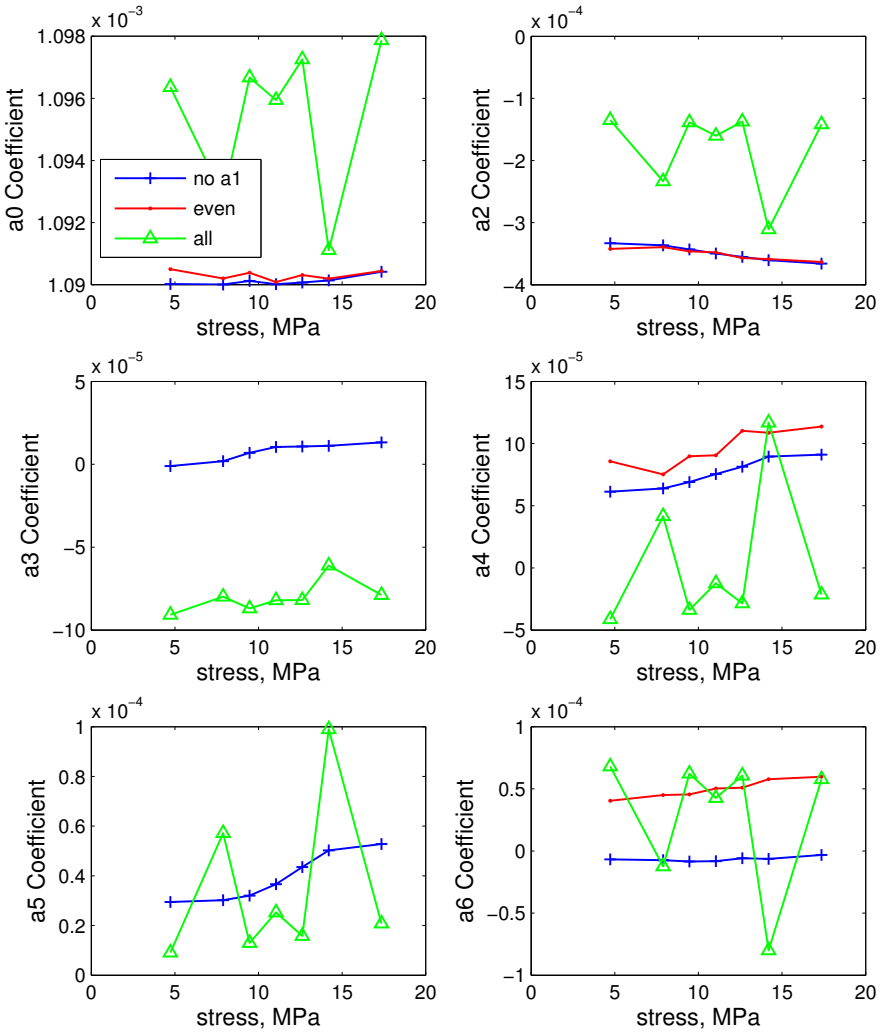

Figure 5.17. Legendre polynomial coefficients across a range of stresses for Double Power Law simulations of n1 = 1 and n2 = 5. Green triangles show coefficients from fitting the deformed sphere with only even terms of the Legendre polynomial. Red dots show the coefficient found using all terms of the Legendre polynomial. Blue asterisks display the coefficients from the Legendre polynomial with all terms except a_1. The mechanism transition range is between 8-18 MPa, as shown in Figure 5.7.

5.4.4 Results for the Full Sphere

Applying Legendre polynomial curve fitting to one quadrant of the sphere does not impose constraints of symmetry. While fitting to one quadrant of the deformed

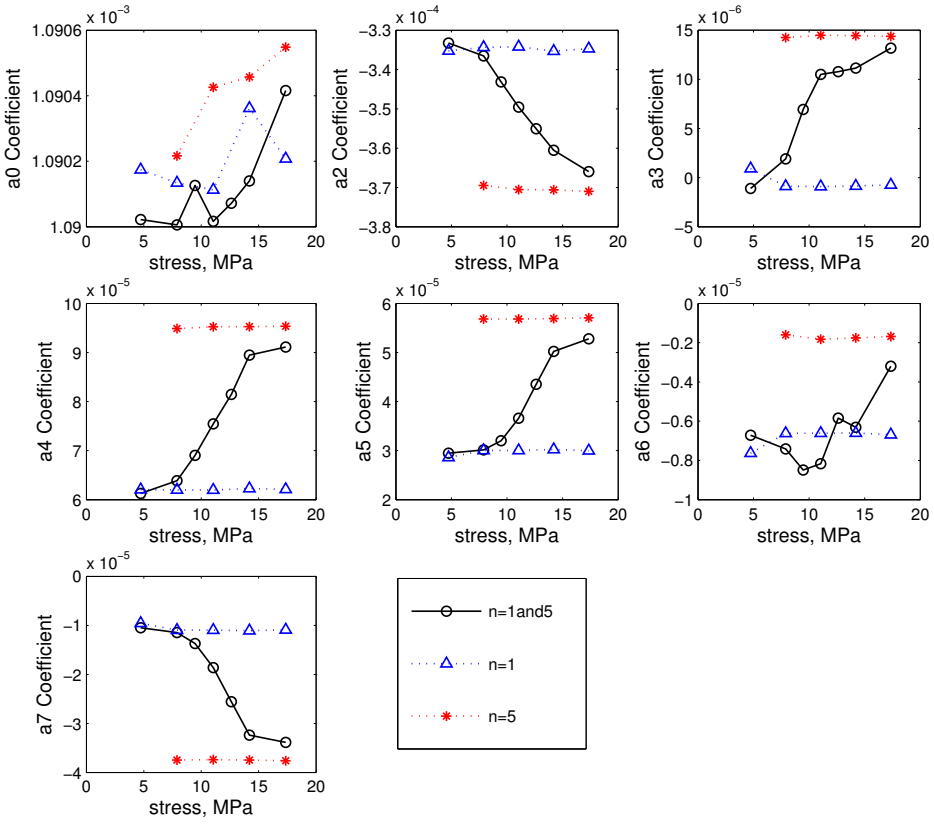

Figure 5.18. Legendre polynomial coefficients from curve fitting the edge of one quarter of the deformed sphere with 7 terms excluding a_1. Results from simulations of of n = 1 and 5 are shown here. The mechanism transition range is between 8 and upwards of 18 MPa, as shown in Figure 5.7.

sphere produced results with excellent R^2 values and great patterns across the range of stresses, these results are not practical for application to experimental results. The Legendre polynomials must be fit to the entire 360° of the deformed shape. To study the Legendre polynomial fitting on the full sphere, the numerical results found in the previous section were reflected and rotated about the axes to complete the sphere.

As in the latter half of the previous section, three Legendre series were investigated, each one with seven terms. The series are the same as those listed in equations 5.12 - 5.14. The coefficient of determination was examined again as a measurement of the

quality of the fit. The values for the three choices of Legendre series are shown in Figure 5.19, for the mixed dominance case of n1 = 1 and n2 = 2.

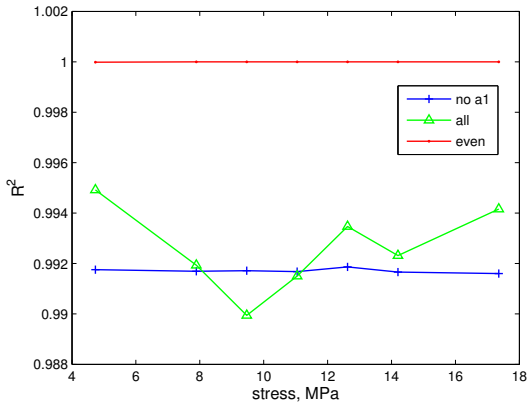

Figure 5.19. The coefficient of determination for various Legendre series fits to the edge of the full deformed sphere. These are from curve fitting n1 = 1 and n2 = 6 simulations with the Double Power Law Model. The Legendre series used for these fits are given by Equations 5.12-5.14.

The trends in R^2 values for the full sphere are different from those found with fitting the Legendre series to the edge of one quadrant of the sphere. This change in trends is expected due to the newly imposed constraints from the symmetry of the sphere. For the full sphere, the series with even terms only returns the strongest fits to the data, with a very consistent R^2 value very close to one. The R^2 values for the series with all terms except a_1 is also very constant across the range of stresses, but has a lower value than the series with only even terms. Finally, the series with all terms returns highly variable R^2 values across the range of stresses. Removing the a_1 term removes the variability in the values, as shown by the blue curve.

It should be noted that the Legendre polynomials with all terms, and with all terms except a_1 are asymmetrical about the equator. Despite the lack of symmetry across the equator, the coefficients of determination for all terms without a_1 still point to an excellent fit to the data by use of this Legendre series. The curve fit done with

even terms only gives an axisymmetric, as well as mirror symmetric curve about the equator.

Again, the trends in the coefficients were examined for each of the fits. The coefficient fits for the series with only even terms and with all terms except a_1 are shown in Figures 5.20 and 5.21, respectively. The coefficients for the series with all terms is not included, as the R^2 values were indicative of a poorer fit. It is illustrated that although the series with only even terms provides the best fit to the data, according to the coefficient of determination results, the patterns in the coefficients are not overwhelmingly obvious. The patterns in coefficients when all terms except a_1 are used are much more distinct, as seen in Figure 5.21.

These coefficients provide a determining factor in distinguishing between single and double mechanisms occurring at the same time. From a single experiment, the creep regime in which the deformation occurs can be determined. By running a complete set of numerical simulations across the full range of stresses, for single and double mechanism creep, the six Legendre coefficients can be determined. The shape of the deformed sample found experimentally can be fit using the Legendre polynomial least-squares fitting technique. The coefficients determined from experimental data can be compared to the full set of theoretical coefficients, for example those found in Figures 5.15, 5.18 and 5.20. By matching the experimentally determined coefficients to the appropriate coefficients at the correct stress, the regime of creep mechanism can be determined. This method can be used to distinguish between single and double mechanisms occurring in the sample.

5.4.5 Shifting Origin

In previous work using Legendre Polynomial curve fitting it was determined that the origin of the function affected the quality of the fit. A surface plot of the $1 - R^2$ values is shown in Figure 5.22, illustrating the possible locations of the origin of the

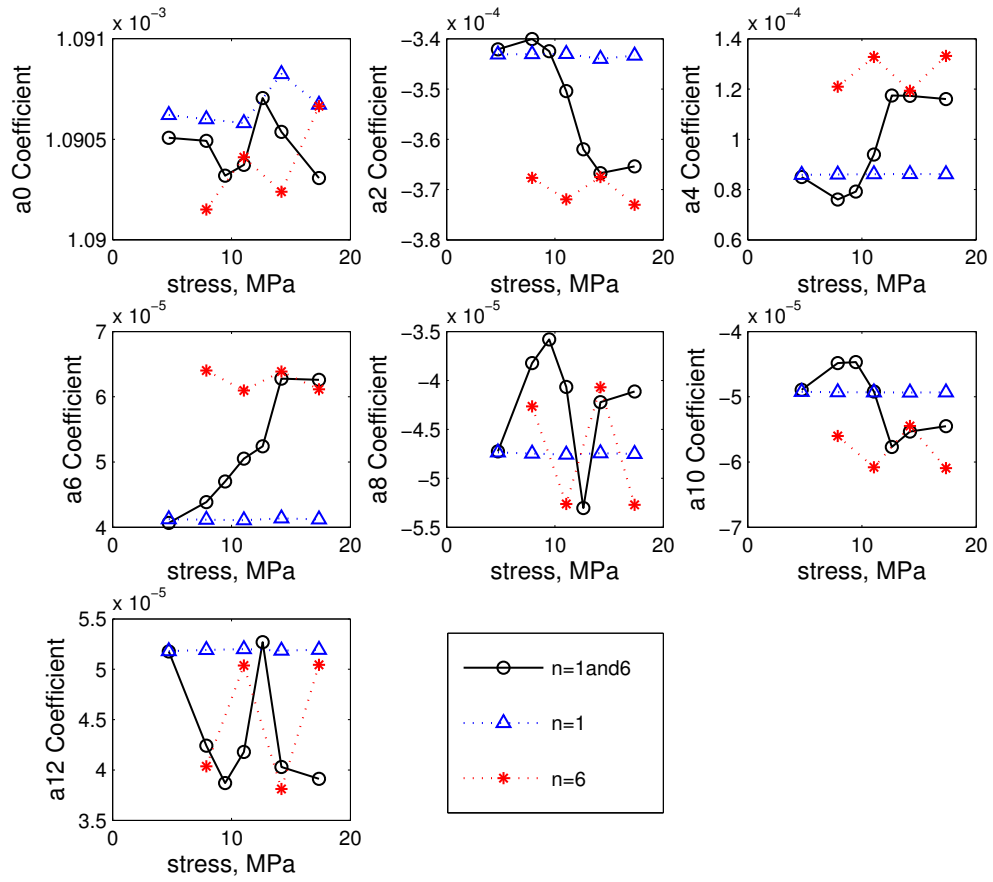

Figure 5.20. Legendre polynomial coefficients from curve fitting the edge of the full deformed sphere with the series of only even terms given in Equation 5.12. Results from simulations of of n = 1 and 5 are shown here. The mechanism transition range is between 8 and upwards of 18 MPa, as shown in Figure 5.7.

Legendre Polynomial fit. There exists a clear saddle directly around the centroid, shown in red, indicating a poor fit. Four regions of stability surround the origin, and are shown in blue. These locations are all good candidates for an origin that will produce a good fit. It was determined that a subtraction of 50 pixels in the y-direction, about 20% of the sample's diameter, from the origin produces the best values.

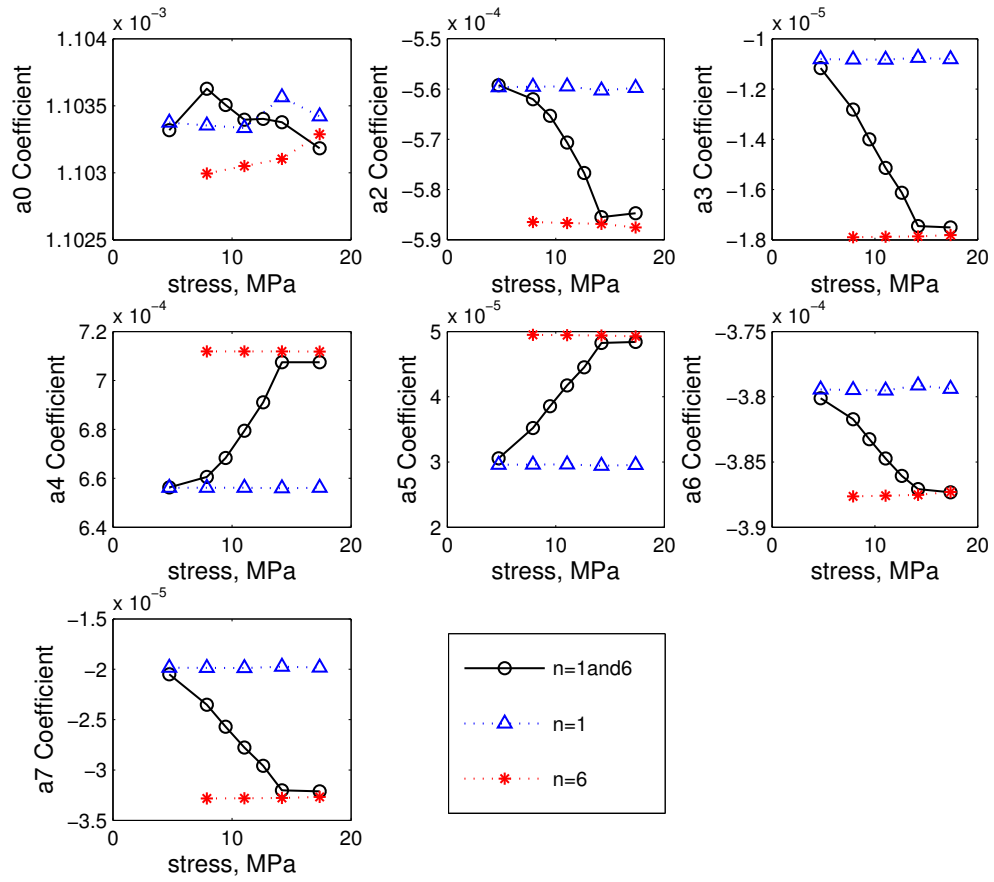

Figure 5.21. Legendre polynomial coefficients from curve fitting the edge of the full deformed sphere with the series of all terms except given in Equation 5.12. Results from simulations of of n = 1 and 5 are shown here. The mechanism transition range is between 8 and upwards of 18 MPa, as shown in Figure 5.7.

To examine the effect of origin location on the quality of the fit to the edge of the numerically generated results in the current work, a series of analyses were performed. The origin of the Legendre Polynomial was shifted in increments of 0.025mm in both the x and y directions. A least-squares fitting routine using the Levenberg-Marquardt optimization routine was implemented to determine the Legendre Polynomial fit to the edge of the deformed sphere. The goodness of fit was quantified with R^2 values. Finally, a surface plot of the $1 - R^2$ values was produced on the grid of possible

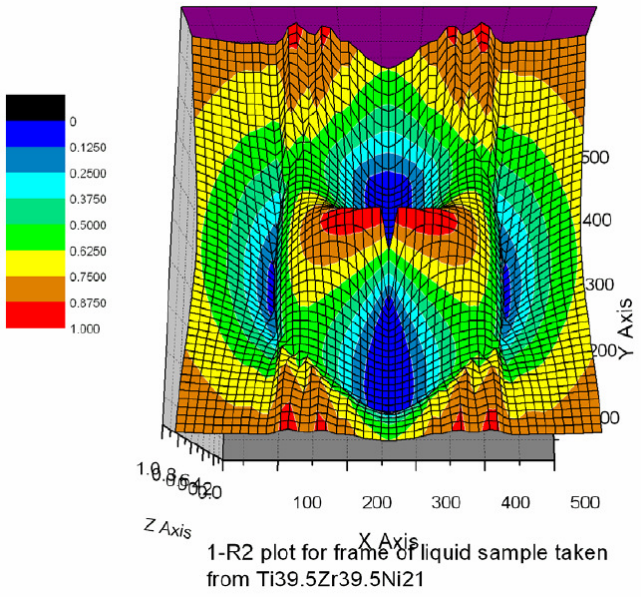

Figure 5.22. R^2 values for the Legendre polynomial fits for a shifted origin [6].

origin locations for the Legendre Polynomial. This process was carried out for the three choices of Legendre series discussed in a previous subsection. The $1-R^2$ surface plots for Legendre series with all terms, only even terms and finally all terms omitting a_1 are shown in Figure 5.23.

The surface plot of the $1 - R^2$ values for the Legendre Polynomial fits using all terms in the series is shown at the top of Figure 5.23. Overall, this surface plot illustrates that the Legendre Polynomial has a generally good fit over the entire range of origin shifts studied in the current work. The variation in values is not smooth across the range of shifted origins, but the amplitude of the variation is not large. The value never exceeds 4 x 10^{-3}, indicating that an origin shift under this selection of Legendre series does not greatly effect the goodness of fit. The middle surface plot shows the $1 - R^2$ values for the Legendre Polynomial composed of only even terms. The shape of the curve is best described as a half pipe, in which the trough runs along the x-axis. The final plot, of the Legendre series with all terms except a_1, shares many

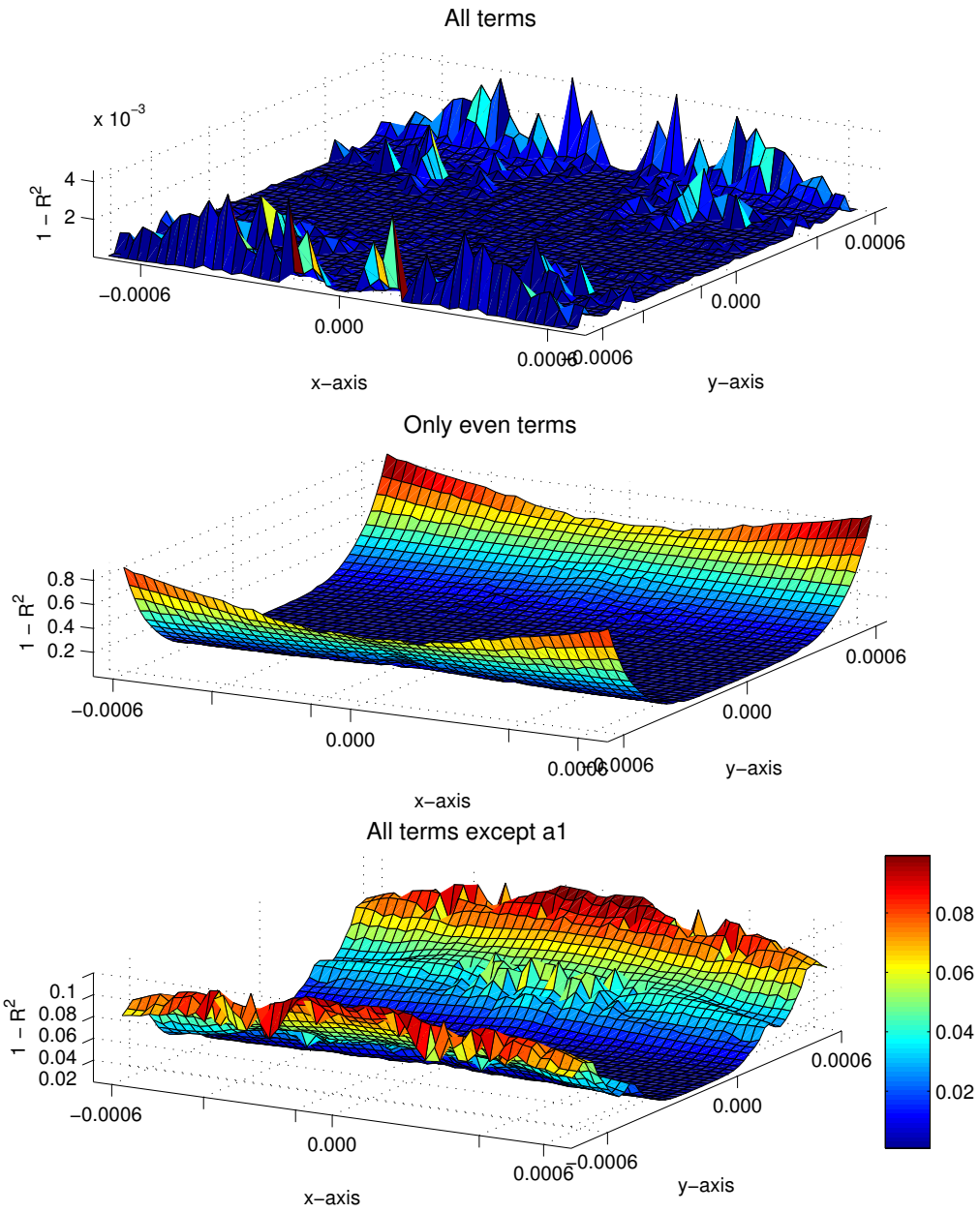

Figure 5.23. $1 - R^2$ values for the Legendre polynomial fits to the edge of the deformed sphere. Top, values from using a 6th order Legendre polynomial with all terms. Middle, using a 6th order Legendre polynomial with only even terms. Bottom, all terms except a_1.

of the same attributes as the middle plot. It too has a half pipe shape, with a trough along the x-axis, but lacks the smoothness of the previous plot. Both of these plots indicate that shifting the origin along the x-axis does not greatly alter the quality of the fit, but moving the origin in the y-direction away from the x-axis reduces the quality of the fit. Keeping the origin of the fit at the centroid of the deformed sphere is perfectly suitable for all three choices of Legendre series, and furthermore is the simplest way to carry out the analysis.

CHAPTER 6

CONCLUSIONS

A 2-D finite element model of Norton creep was developed for a rotating sphere. This model greatly reduced the computation time for simulating the creep behavior of a rotating sphere. Excellent agreement was found between the new model and the 3-D FEA model developed in the previous work. Furthermore, the 2-D Norton creep model gave results that showed excellent agreement with experimental results found in the literature [38].

Next, a 2-D Double Power Law model was developed. The model allows for the study of creep behavior of a rotating sample in regimes of mixed creep mechanism dominance. The model was validated against the group's previous FEA model, as well as experimental data in a region of transitioning mechanisms in pure aluminum [38]. Excellent agreement was found between the theory and the experimental results of Harper and Dorn across the entire range of stresses.

The FEA Norton and Double Power Law models were used to identify and characterize the regimes of mixed creep mechanism dominance. Various analyses were carried out, including examination of the stress versus strain rate, radius ratio, apparent stress exponent and Legendre polynomial curve fitting. The radius ratio in the regimes of mixed dominance was found to vary between the radius ratios given by the single mechanism cases. Similarly, the apparent stress exponent in the region of mixed dominance was shown to be bounded by the two individual stress exponents.

Legendre polynomials were fit the to edge of the deformed spheres. It was determined that omitting the coefficient a_1 from Legendre series provided the best fit to

the edge of one quadrant of the deformed sphere. The same choice of series was shown to provide excellent fits to the edge of the entire sphere as well. The Legendre series with all terms except a_1 provided distinct patterns in coefficient values across the range of stresses. Fitting Legendre polynomials to the edge of the deformed spheres was shown to be an effective method of identifying the dominating mechanism given a set of Legendre coefficients.

From a single experiment the creep regime can be determined from comparison of the experimental and theoretical Legendre polynomial coefficients. These numerically generated Legendre coefficients can be compared to experimental data analyzed using Legendre polynomial curve fitting to determine the active creep mechanism in a sample. Not only do Legendre polynomials offer a further method of quantifying the regions of mechanism transition, but also provides a tool for extracting the regime of creep dominance in a given sample.

APPENDIX A

ANSYS USER-SUBROUTINE: USERCREEP.F

```
*deck,usercreep       parallel  user                                    gal
      SUBROUTINE usercreep (impflg, ldstep, isubst, matId , elemId,
     &                      kDInPt, kLayer, kSecPt, nstatv, nprop,
     &                      prop  , time  , dtime , temp  , dtemp ,
     &                      toffst, Ustatev, creqv , pres  , seqv  ,
     &                      delcr , dcrda)
c*************************************************************************
c     *** primary function -- adapted for use by Maija ***
c           Define creep laws when creep table options are
c           TB,CREEP with TBOPT=100.
c           Demonstrate how to implement usercreep subroutine
c
c            Creep equation is
c               dotcreq := (k1 * seqv ^ n1 + k2 * seqv ^ n2) * exp (-b/T)
c
c               seqv  is equivalent effective stress (Von-Mises stress)
c               creqv is equivalent effective creep strain
c               T     is the temperature
c               k1, k2, m, n1, n2, b are materials constants,
c
c           This model corresponds to  double power law creep
c
c                                                          gal 10.01.1998
c
c*************************************************************************
c
c     input arguments
c     ===============
c      impflg   (in ,sc   ,i)            Explicit/implicit integration
c                                        flag (currently not used)
c      ldstep   (in ,sc   ,i)            Current load step
c      isubst   (in ,sc   ,i)            Current sub step
c      matId    (in ,sc   ,i)            number of material index
c      elemId   (in ,sc   ,i)            Element number
c      kDInPt   (in ,sc   ,i)            Material integration point
c      kLayer   (in ,sc   ,i)            Layer number
c      kSecPt   (in ,sc   ,i)            Section point
c      nstatv   (in ,sc   ,i)            Number of state variables
```

```
c      nprop    (in ,sc   ,i)             size of mat properties array
c
c      prop(1)              A1, first coefficient
c      prop(2)            n1, first stress exponent
c      prop(3)              A2, second coefficient
c      prop(4)              n2, second stress exponent
c      prop(5)              (-b/T), 55326
c
c      time                                Current time
c      dtime                               Current time increment
c      temp                                Current temperature
c      dtemp                               Current temperature increment
c      toffst   (dp, sc,   i)             temperature offset from
c                                          absolute zero
c      seqv     (dp ,sc  , i)             equivalent effective stress
c      creqv    (dp ,sc  , i)             equivalent effective creep strain
c      pres     (dp ,sc  , i)             hydrostatic pressure stress,
c                                          -(Sxx+Syy+Szz)/3
c
c     input output arguments               input desc     / output desc
c     =====================                ==========       ===========
c      Ustatev  (dp,ar(*), i/o)            user defined internal state
c                                          variables at
c                                          time 't' / 't+dt'.
c                                          This array will be passed
c                                          in containing the
c                                          values of these variables
c                                          at start of the
c                                          time increment. They must
c                                          be updated in this
c                                          subroutine to their values
c                                          at the end of
c                                          time increment, if any of
c                                          these internal
c                                          state variables are associated
c                                          with the
c                                          creep behavior.
c
c     Ustatev(1)
c
c
c     output arguments
c     ================
c      delcr    (dp ,sc  , o)             incremental creep strain
c      dcrda    (dp,ar(*), o)             output array
c                                          dcrda(1) - derivative of
c    incremental creep
```

```
c                                                       strain to effective
c    stress
c                                          dcrda(2) - derivative of
c    incremental creep
c                                                       strain to creep
c    strain
c
c     local variables
c     ===============
c      c1,c2,c3,c4,c5 (dp, sc, 1)         temporary variables as creep
c constants
c      con1        (dp ,sc, 1)            temporary variable
c      t           (dp ,sc, 1)            temporary variable
c
c**********************************************************************
c
c --- parameters
c
#include "impcom.inc"

      DOUBLE PRECISION ZERO
      PARAMETER        (ZERO = 0.0d0)
c
c --- argument list
c
      INTEGER          ldstep, isubst, matId , elemId,
     &                 kDInPt, kLayer, kSecPt, nstatv,
     &                 impflg, nprop
      DOUBLE PRECISION dtime , time  , temp  , dtemp , toffst,
     &                 creqv , seqv  , pres
      DOUBLE PRECISION prop(*), dcrda(*), Ustatev(nstatv)
c
c --- local variables
c
      DOUBLE PRECISION c1    , c2    , c3    , c4    , c5    ,
     &                 con1  , delcr , t
c
c**********************************************************************
c
c *** skip when stress and creep strain are all zero
      if (seqv.LE.ZERO.AND.creqv.LE.ZERO) GO TO 990
c *** add temperature off set
      t       = temp + toffst
c *** Steady State Creep Law
c        delcr := (a1 * seqv ^ n1 + a2 * seqv ^ n2) * exp (-b/T) * dtime
      c1      = prop(1)
      c2      = prop(2)
```

```
      c3      = prop(3)
      c4      = prop(4)
      c5      = prop(5)
c *** user need to make sure if para(5) has nonzero value,
c                                          temperature should be also nonzero.
      con1    = ZERO
      if(c5.ne.ZERO .and. t.gt.ZERO) con1 = exp(-c5/t)
c *** calculate incremental creep strain
      delcr   = ZERO
      IF(c1.gt.ZERO .OR. c3.gt.ZERO) delcr = delcr + (((c1 * seqv**c2) +
     &               (c3 * seqv**c4)) * con1 * dtime)
c *** derivitive of incremental creep strain to effective stress
      dcrda(1)= ((c1 * c2 * seqv**((c2)-1)) +
     &               (c3 * c4* seqv**((c4)-1))) * con1 * dtime
c *** derivitive of incremental creep strain to effective creep strain
c *** not need for this creep law
      dcrda(2) = ZERO
c *** write the effective creep strain to last state variable for verification
      Ustatev(nstatv) = creqv + max(delcr, ZERO)
 990  continue
      return
      end
```

APPENDIX B

EXAMPLE ANSYS INPUT FILE

Here is an example of an ANSYS input file used for in this research. This code simulates the rotation of a 1mm radius sphere of pure niobium, and provides information about the deformation behavior in regimes of mixed creep dominance.

```
/GO
/COM,
/COM,Preferences for GUI filtering have been set to display:
/COM,  Structural
/CLEAR
/FILNAME,AnalysisDouble
/PREP7
! Based on 3-D creep analysis J. Lee 2007, modified by X. Ye 2010
! 2-D with Double Power Law Creep, M. Benitz 7/2010

!------------ SET PARAMETERS -------------

*SET,ANG_VELO,40847
*SET,TEMPER,2258.15
*SET,RHO,8562
*SET,I,1
*SET,J,1
*SET,ZCOEFF,5E-2
*SET,ZSEXP,1
*SET,ZCOEFF2,6E-37
*SET,ZSEXP2,5
*SET,ZSTRAIN,0.11
*SET,ZR,0.001
*SET,ZUREQ,ZR*ZSTRAIN
*SET,ZUREQSUB,ZR*ZSTRAIN*0.94

!------------ MATERIAL PROPERTIES ---------

MPTEMP,,,,,,,,
MPTEMP,1,0
```

```
MPDATA,EX,1,,1.03E11
MPDATA,PRXY,1,,0.38
MPTEMP,,,,,,,,
MPTEMP,1,0
MPDATA,DENS,1,,RHO

TB,CREEP,1,1,5,100
TBTEMP,0
TBDATA,,ZCOEFF,ZSEXP,ZCOEFF2,ZSEXP2,55326,,,
! item 4 is (activation energy for creep divided by R),
! units K. Set to zero for temperature-independent (exp(0)=1)

!------------ CREATE SPHERE ---------
CYL4,0,0,ZR,0,0,90

!-------- SELECT ELEMENT TYPE --------
ET,1,PLANE183,0,,1
! KEYOPT(1) = 0 -> quadrilateral
! KEYOPT(3) = 1 -> axisymmetric

!----------- CREATE MESH --------------
ESIZE,0.0001
TYPE,   1
MAT,       1
REAL,   1
ESYS,       0
SECNUM,

MSHAPE,0,2D
MSHKEY,0
ASEL,ALL
AMESH,ALL

!------------- APPLY BOUNDARY CONDITIONS ---------
TUNIF,TEMPER

NSEL,S,LOC,Y,0
D,ALL,UY,0
NSEL,S,LOC,X,0
D,ALL,UX,0
ALLSEL,ALL

!------------- INITIAL CONDITION FOR TRANSIENT ANALYSIS ---------
/SOLU
ANTYPE,TRANS
TIMINT,OFF
SOLCONTROL,1
```

```
AUTOTS,1
RESCONTROL,DEFINE,ALL,1,1
LNSRCH,0
CNVTOL,F, ,0.00005,2,0.01,
RATE,1
TIME,1
SOLVE
FINISH

/SOLU
TIMINT,ON

!------------- DO LOOP STARTS ON I ---------------------

*DO,I,100,400000,100

OMEGA,0,ANG_VELO,0,0
SOLCONTROL,1
NLGEOM,1
RESCONTROL,DEFINE,ALL,1,1
LNSRCH,0
RATE,1
CNVTOL,F, ,0.00005,2,0.01,
DELTIM,50
AUTOTS,1
TIME,I

SOLVE

!------------- STORE THE CURRENT TIME --------------
*SET,DEG4TIME,I

!------------- STORE DISPLACEMENTS OF NODES ON MERIDIAN --------
*GET,UY_N_POLE,NODE,2,U,Y
*GET,UX_EQUATOR,NODE,1,U,X

!---------------------------------------
!------IF RADIAL DISPLACEMENT IS GREATER THAN
! -----------------SUBORDINATE TARGET THEN DECREASE STEP SIZE ------

*IF,UX_EQUATOR-ZR,GT,ZUREQSUB,THEN

*DO,J,DEG4TIME+2,20000,10

OMEGA,0,0,ANG_VELO,0
SOLCONTROL,1
NLGEOM,1
```

```
RESCONTROL,DEFINE,ALL,1,1
LNSRCH,0
RATE,1
CNVTOL,F, ,0.00005,2,0.01,
DELTIM,5
AUTOTS,1
TIME,J

SOLVE

!------STORE THE CURRENT TIME --------------
*SET,DEG4TIME,J

!-----STORE DISPLACEMENTS OF NODES ON MERIDIAN --------------
*GET,UY_N_POLE,NODE,2,U,Y
*GET,UX_EQUATOR,NODE,1,U,X

!------IF RADIAL DISPLACEMENT IS GREATER
!-------------THAN TARGET THEN EXIT THE CURRENT LOOP -----
*IF,UX_EQUATOR,GT,ZUREQ,EXIT

*ENDDO

*ENDIF

*IF,UX_EQUATOR,GT,ZUREQ,EXIT

*ENDDO


!----------------- SAVE PARAMETERS -------------------

PARSAV,SCALAR,PARAMETERS,TXT

FINISH



/POST26
NSOL,UX_EQUATOR,NODE,1,U,X
PRVAR,DEG4TIME,UX_EQUATOR,UY_NPOLE
FINISH

SAVE,'n1n6_3mpa_time','DB','C:\Documents and Settings\Maija\My Documents'
```

BIBLIOGRAPHY

[1] Allen, N.P., and Carrington, W.E. Exploratory creep tests on metals of high melting point. *Institute of Metals 82*, 11 (1954), 525–533.

[2] Arfken, George B., and Weber, Hans J. *Mathematical Methods for Physicists*, 4 ed. Academic Press, San Diego, 1995.

[3] Armstrong, D.J., Murray, D., and Hopkin, L.M.T. Techniques for creep testing at high temperatures. *Journal of Less-Common Metals 1* (1959), 125–131.

[4] Atkinson, A.W. New high temperature materials. *Metals and Materials 8* (1992), 99–102.

[5] Bakhtiyarov, S.I., and Overfelt, R.A. Thermophysical property measurements by electromagnetic levitation melting technique under microgravity. *Annals of the New York Academy of Sciences 974* (2002), 132–145.

[6] Bradshaw, R.C. Machine vision for automated data reduction in containerless density measurements. Master's thesis, University of Massachusetts, 2004.

[7] Bradshaw, R.C., Hyers, R.W., Rogers, J.R., Rathz, T.J., Lee, G.W., Gangopadhyay, A.K., and Kelton, K.F. Non-contact techniques and measurements of density of quasicrystal-forming Ti-Zr-Ni alloy melts. *Annals of the New York Academy of Sciences 1077* (2006), 63–74.

[8] Bradshaw, R.C., Schmidt, D.P., Rogers, J.R., Kelton, K.F., and Hyers, R.W. Machine vision for high precision volume measurement applied to levitated containerless materials processing of $Ti_{30}Zr_{30}Ni_{40}$. *Review of Scientific Instruments 76*, 12 (2005).

[9] Brandt, E.H. Levitation in physics. *Science 243*, 4889 (1989), 349–355.

[10] Buckman, R.W. The creep behavior of refractory metal alloys. *International Journal of Refractory Metals & Hard Materials 18* (2000), 253–257.

[11] Carroll, D.F., and Wiederhorn, S.M. High temperature creep testing of ceramics. *International Journal of High Technology Ceramics 4* (1988), 227–241.

[12] Courtney, T. *Mechanical Behavior of Materials*. McGraw-Hill Co., Boston, MA, 2000.

[13] Damaschke, B., Oelgeschlaeger, D., Ehrich, J., Dietzsch, E., and Samwer, K. Thermal expansion measurements of liquid metallic samples measured under microgravity condition. *Review of Scientific Instruments 69* (1998), 2110–2113.

[14] Damaschke, B., and Samwer, K. Thermal expansion measurements of glass-forming alloys in the melt and undercooled state under microgravity conditions. *Applied Physics Letters 75* (1999), 2220–2222.

[15] Egry, I., Lohofer, G., Seyhan, I., Schneider, S., and Feuerbacher, B.F. Viscosity and surface tension measurements in microgravity. *International Journal of Thermophysics 20*, 4 (1999), 1005–1015.

[16] El-Mehairy, A.E., and Ward, R.G. A new technique for determination of density of liquid metals: Application to copper. *Transactions of The Metallurgical Society of AIME 227* (1963), 1226–1229.

[17] Enderby, J.E., and Ansell, S. The electrical conductivity of levitated liquids. *Applied Physics Letters 71*, 1 (1997), 116–118.

[18] Endo, T., and Sakon, T. Creep-fatigue life prediction using simple high-temperature low-cycle fatigue testing machines. *Metals Technology 11* (1984), 489–496.

[19] Green, W.V. Short-time creep-rupture behavior of tungsten at 2250 to 2800 C. *Transactions of The Metallurgical Society of AIME 215*, 6 (1959), 1057–1060.

[20] Gundarev, S.N., Gurov, A.F., Dement'ev, V.V., Demidov, A.S., Rusanov, A.E., and Khomyakov, A.A. High-temperature creep tests on specimens of single-crystal molybdenum with a complex stressed state. *Strength of Materials 22*, 7 (1991), 1012–1015.

[21] Heyes, J.G., and Sellors, R.G.R. High temperature applications of refractory metals. *Metals and Materials 8* (1992), 86–92.

[22] Hyers, R.W., Bradshaw, R.C., Rogers, J.R., Rathz, T.J., Lee, G.W., Gangopadhyay, A.K., and Kelton, K.F. Surface tension and viscosity of quasicrystal-forming Ti-Zr-Ni alloys. *International Journal of Thermophysics 25*, 4 (2004), 1155–1162.

[23] Hyers, R.W., Trapaga, G., and Flemings, M.C. The measurement of the surface tension and viscosity of undercooled melts under microgravity conditions. *Conference Preceedings, TMS, Warrendale, Pennsylvania* (1999), 23–31.

[24] Jenkins, M.G. Testing ceramics for creep. *Mechanical Engineering 119*, 2 (1997), 72–76.

[25] Johnson, A.E., and Frost, N.E. Equipment for compression-creep tests at high temperatures. *Engineering 176*, 4562 (1953), 28–29.

[26] Kiessig, H., and Essmann, U. Flow stress of pure niobium between 2200 k and the melting point 2741 k. *Scripta Metallurgica 19* (1985).

[27] Kinsey, H.V. High temperature creep testing. *Canadian Metals and Met. Ind 11*, 6 (1948), 19–22.

[28] Kloc, L., and Fiala, J. On creep behavior of several metallic materials at low stresses and elevated temperatures. *Chemical Papers 53*, 3 (1999), 155–164.

[29] Lee, J. *Non-Contact Measurement of Creep Resistance of Ultra-High-Temperature Materials*. PhD thesis, University of Massachusetts, 2006.

[30] Lee, J., Bradshaw, R.C., Hyers, R.W., Rogers, J.R., Rathz, T.J., Wall, J.J., Choo, H., and Liaw, P.K. Non-contact measurement of creep resistance of ultra-high-temperature materials. *Materials Science and Engineering A 463* (2007), 185–196.

[31] Lee, J., Hyers, R.W., Rogers, J.R., Rathz, T.J., Wall, J.J., Choo, H., and Liaw, P.K. Non-contact measurements of creep properties of niobium at 1985 C. *Review of Scientific Instruments 64*, 10 (1993), 1–26.

[32] Lindblom, J., Seitisleam, F., and Henderson, P.J. Creep testing of steels at very high temperatures. *Journal of Testing and Evaluation 24*, 5 (1996), 329–332.

[33] Lipetzky, P. Refractory metals: A primer. *JOM 54*, 3 (2002), 47–49.

[34] Lohofer, G., Schneider, S., and Egry, I. Thermophysical properties of undercooled liquid $Co_{80}Pd_{20}$. *International Journal of Thermophysics 22*, 2 (2001), 593–604.

[35] Lyman, T., Boyer, H.E., Unterweiser, P.M., Foster, J.E., Hontas, J.P., and Lawton, H. *Metals Handbook*. 1961.

[36] McGill, I.R. Intermetallic compounds of the platinum group metals. *Platinum Metals Review 21*, 3 (1977), 85–89.

[37] Meschter, P.J., and Schwartz, D.S. Silicide-matrix materials for high-temperature applications. *JOM 41*, 11 (1989), 52–55.

[38] Murty, K.L., Gollapuri, S., and Charit, I. Newtonian viscous creep in metals. *Transactions of the Indian Institute of Metals 63* (2010), 85–91.

[39] Nabarro, F.R.N., and de Villiers, H.L. *The Physics of Creep: Creep and Creep-resistant Alloys*. Taylor & Francis, London, 1995.

[40] P.-F, Paradis, Yu, T.I.J., Aoyama, T., Yoda, S., and Weber, J.K.R. Contactless density measurement of superheated and undercooled liquid $Y_3Al_5O_12$. *Journal of Crystal Growth 249* (2003), 523–530.

[41] Park, J.J. Creep strength of a tungsten-rhenium-hafnium carbide alloy from 2200 to 2400 K. *Material Science and Engineering A 265* (1999), 174–178.

[42] Peifer, W.A. Levitation melting.....a survey of the state-of-the-art. *Journal of Metals*, 487–493.

[43] Rhim, W.-K., Chung, S.K., Barber, D., Man, K.F., Gutt, G., Rulison, A., and Spjut, R.E. An electrostatic levitator for high-temperature containerless materials processing in 1-g. *Review of Scientific Instruments 64*, 10 (1993), 2961–2970.

[44] Rhim, W.-K., Ohsaka, K., Paradis, P.-F., and Spjut, R.E. Noncontact technique for measuring surface tension and viscosity of molten materials using high temperature electrostatic levitation. *Review of Scientific Instruments 70*, 6 (1999), 2796–2801.

[45] Rogers, J.R., Hyers, R.W., Rathz, T., Savage, L., and Robinson, M.B. Thermophysical property measurement and materials research in the NASA/MSFC electrostatic levitator. *Conference Preceedings, American Institute of Physics Space Technology and Applications International Forum, Albuquerque, NM 552* (2001), 332–336.

[46] Rulison, A.J., Watkins, J.L., and Zambrano, B. Electrostatic containerless processing system. *Review of Scientific Instruments 68*, 7 (1997), 2856–2863.

[47] Saboungi, M.-L., J. Enderby, B. Glorieux, Schnyders, H., Sungaila, Z., Krishnan, S., and Price, D.L. What is new of the levitation front? *Journal of Non-Crystalline Solids 312* (2002).

[48] Sadananda, K., Feng, C.R., Mitra, R., and Deevi, S.C. Creep and fatigue properties of high temperature silicides and their composites. *Materials Science and Engineering A 261*, 1 (1999).

[49] Saito, T., Shiraishi, Y., and Sakuma, Y. Density measurement of molten metals by levitation technique at temperatures between 1800 and 2200 C. *Transactions of the Iron and Steel Institute of Japan 9* (1969), 118–126.

[50] Schneibel, J.H., and Lin, H.T. Creep properties of molybdenum silicide intermetallics containing boron. *Materials at High Temperatures 19*, 1 (2002), 25–28.

[51] Shiraishi, S.Y., and Ward, R.G. The density of nickel in the superheated and supercooled states. *Canadian Metallurgical Quarterly 3*, 1 (1964), 117–122.

[52] Song, H.-S., Kim, E.-P., Lee, S., Noh, J.-W., , and Baek, W.-H. Effect of Ni/Fe ratio on the mechanical properties for tungsten heavy alloy. *Conference Preceedings, The 1992 Powder Metallurgy World Congress. Part 6 (of 9), San Francisco, CA* (1992), 77–83.

[53] Swanson Analysis Systems, Inc. *ANSYS User's Manual*, 1994.

[54] Wright, P.K. The high temperature creep behavior of doped tungsten wires. *Metallurgical Transactions A 9* (1978).

[55] Yamabe-Mitarai, Y., Gu, Y., Huang, C., Volkl, R., and Harada, H. Platinum-group-metal-based intermetallics as high-temperature structural materials. *JOM 56*, 9 (2004), 34–39.

[56] Zhu, S.M., Fahrenholtz, W.G., , and Hilmas, G.E. Enhanced densification and mechanical properties of ZrB_2-SiC processed by a preceramic polymer coating route. *Scripta Materialia 59* (2008), 123–126.